

## CANCER

# Metabolic adaptation of ovarian tumors in patients treated with an IDO1 inhibitor constrains antitumor immune responses

Kunle Odunsi<sup>1,2,3\*</sup>, Feng Qian<sup>1,2,3</sup>, Amit A. Lugade<sup>3</sup>, Han Yu<sup>4</sup>, Melissa A. Geller<sup>5</sup>, Steven P. Fling<sup>6</sup>, Judith C. Kaiser<sup>6</sup>, Andreeanne M. Lacroix<sup>6</sup>, Leonard D'Amico<sup>6</sup>, Nirasha Ramchurren<sup>6</sup>, Chihiro Morishima<sup>6,7</sup>, Mary L. Disis<sup>6</sup>, Lucas Dennis<sup>8</sup>, Patrick Danaher<sup>8</sup>, Sarah Warren<sup>8</sup>, Van Anh Nguyen<sup>9</sup>, Sudharshan Ravi<sup>10</sup>, Takemasa Tsuji<sup>1,2,3</sup>, Spencer Rosario<sup>4</sup>, Wenjuan Zha<sup>4</sup>, Alan Hutson<sup>4</sup>, Song Liu<sup>4</sup>, Shashikant Lele<sup>11</sup>, Emese Zsiros<sup>3,11</sup>, A. J. Robert McGray<sup>3</sup>, Jessie Chiello<sup>3</sup>, Richard Koya<sup>1,2,3</sup>, Thinkle Chodon<sup>1,2,3</sup>, Carl D. Morrison<sup>12</sup>, Vasanta Putluri<sup>13</sup>, Nagireddy Putluri<sup>13</sup>, Donald E. Mager<sup>9,14</sup>, Rudiyanto Gunawan<sup>10</sup>, Martin A. Cheever<sup>6†</sup>, Sebastiano Battaglia<sup>3</sup>, Junko Matsuzaki<sup>1,2,3\*</sup>

To uncover underlying mechanisms associated with failure of indoleamine 2,3-dioxygenase 1 (IDO1) blockade in clinical trials, we conducted a pilot, window-of-opportunity clinical study in 17 patients with newly diagnosed advanced high-grade serous ovarian cancer before their standard tumor debulking surgery. Patients were treated with the IDO1 inhibitor epacadostat, and immunologic, transcriptomic, and metabolomic characterization of the tumor microenvironment was undertaken in baseline and posttreatment tumor biopsies. IDO1 inhibition resulted in efficient blockade of the kynurenine pathway of tryptophan degradation and was accompanied by a metabolic adaptation that shunted tryptophan catabolism toward the serotonin pathway. This resulted in elevated nicotinamide adenine dinucleotide (NAD<sup>+</sup>), which reduced T cell proliferation and function. Because NAD<sup>+</sup> metabolites could be ligands for purinergic receptors, we investigated the impact of blocking purinergic receptors in the presence or absence of NAD<sup>+</sup> on T cell proliferation and function in our mouse model. We demonstrated that A2a and A2b purinergic receptor antagonists, SCH58261 or PSB1115, respectively, rescued NAD<sup>+</sup>-mediated suppression of T cell proliferation and function. Combining IDO1 inhibition and A2a/A2b receptor blockade improved survival and boosted the antitumor immune signature in mice with IDO1 overexpressing ovarian cancer. These findings elucidate the downstream adaptive metabolic consequences of IDO1 blockade in ovarian cancers that may undermine antitumor T cell responses in the tumor microenvironment.

## INTRODUCTION

Prevention of autoimmunity or immunopathology via tryptophan (Trp) catabolism is driven by three key enzymes, indoleamine 2,3-dioxygenase 1 (IDO1), its paralog IDO2, and tryptophan 2,3-dioxygenase 2 (TDO). IDO1 catalyzes Trp degradation along the kynurenine (Kyn) pathway, resulting in local reduction of Trp and production of immunosuppressive Trp metabolites (1, 2). Trp depletion leads to an accumulation of uncharged Trp-tRNA in cells, and this activates the integrated stress response kinase, general control

nonderepressible 2, which activates processes that result in blockade of protein synthesis and arresting cell growth (3). In addition, IDO-mediated catabolism of Trp inhibits immunoregulatory kinases, mammalian target of rapamycin, and protein kinase C θ, along with the induction of autophagy (4). Downstream effects of IDO1 enzyme activity to protect tumors from immune attack are mediated by suppression of effector CD8<sup>+</sup> T and natural killer (NK) cells, generation and activation of T regulatory cells (T<sub>regs</sub>) (5) and myeloid-derived suppressor cells, and promotion of tumor angiogenesis (6).

Multiple tumor types express IDO1 at high frequency, and high IDO1-expressing tumors are often associated with reduced CD8<sup>+</sup> T cell infiltration, increased T<sub>regs</sub>, and decreased survival (7). In human epithelial ovarian cancers (EOC), high IDO1 expression was correlated with a reduced number of CD8<sup>+</sup> tumor-infiltrating lymphocytes (TILs) (8), and expression of IDO1 was shown to be correlated with a higher Kyn:Trp ratio in the ovarian tumor microenvironment (TME) (9). In preclinical models, inhibition of IDO1 was shown to synergize with chemotherapy and immune checkpoint inhibitors to mediate rejection of poorly immunogenic tumors (10, 11). Together, these observations provide a strong rationale for therapeutic targeting of the IDO1 pathway to revert tumor-induced immunosuppression in human EOC.

Epacadostat (EPA; INCB024360) is an orally available reversible competitive IDO1 inhibitor with demonstrated immunomodulatory effects on effector T cell and NK cell function and reduced conversion of naïve T cells to T<sub>regs</sub> (12). In the first-in-human dose escalation

Copyright © 2022  
The Authors, some  
rights reserved;  
exclusive licensee  
American Association  
for the Advancement  
of Science. No claim  
to original U.S.  
Government Works

study, there was a dose-dependent reduction in plasma Kyn and Kyn:Trp ratio at all doses and in all patients (13). Compelling pre-clinical evidence suggested a synergistic effect of combined IDO1 and checkpoint blockade compared to checkpoint blockade alone (10), leading to several promising multidisease phase 1/2 clinical studies testing EPA combined with pembrolizumab or nivolumab (ECHO-202 and ECHO-204) (14, 15).

However, failure to observe a substantial benefit from the randomized phase 3 ECHO-301 clinical trial in patients with melanoma (16) has dampened enthusiasm for IDO1 inhibitors in cancer immunotherapy and suggests that there is still a gap in knowledge about IDO1 biology in the TME and the metabolic consequences from its blockade. Several possible reasons for the failure of EPA have been proposed, including insufficient inhibition of IDO1 within the tumor, potential for compensatory immune escape via tumor production of TDO, and activation of downstream effector pathways such as aryl hydrocarbon receptor (17, 18).

To examine the intratumoral effects of IDO1 inhibition, we designed a “window-of-opportunity” study using baseline and posttreatment tissue biopsies to examine the immunological and metabolic effects of neoadjuvant EPA in patients with newly diagnosed advanced high-grade serous ovarian cancer. The primary objective of the pilot study was to determine whether EPA promotes CD8<sup>+</sup> TIL accumulation. We also assessed immunogenomic and metabolic changes from IDO1 blockade and uncovered metabolic adaptation in the TME that shunted Trp catabolism toward the serotonin pathway and elevated nicotinamide adenine dinucleotide (NAD<sup>+</sup>) biosynthetic pathways, which was detrimental for T cell proliferation and function. We showed that NAD<sup>+</sup> suppressed T cell function via A2a and A2b purinergic receptors, and the combination of IDO inhibition and A2a/A2b receptor blockade improved survival in a preclinical mouse model of ovarian cancer.

## RESULTS

### Study design and safety profile of neoadjuvant EPA

Baseline biospecimens were collected from consented patients with newly diagnosed EOC. Upon completion of 2-week oral EPA regimen (600 mg twice a day), patients underwent standard tumor debulking surgery (fig. S1A). The EPA regimen and dose were previously shown to be well tolerated and effective at normalizing Kyn:Trp ratios (13). During surgery, posttreatment tumor tissue from the geographic area of the initial biopsy was harvested, and ascites fluid was collected if present. After surgery, patients were treated with standard-of-care platinum-based chemotherapy. The clinical trial (NCT01685255) enrolled 17 chemotherapy-naïve patients with EOC (table S1) between August 2014 and November 2015. The primary end point of the study was to determine whether EPA altered the number of CD8<sup>+</sup> T cells in the TME. Secondary objectives included safety and tolerability, impact of EPA on Kyn/Trp ratios, gene expression in the TME, and frequency and phenotype of TILs. We performed post hoc metabolomic analyses to understand impacts of EPA on downstream Trp catabolism beyond Kyn.

There were no new or dose-limiting toxicities in any patient (table S2). The most common treatment-related grade 3 or 4 toxicities were anemia (36%), hypotension (14%), neutropenia (7%), and lymphopenia (7%). The investigational therapy with EPA did not result in treatment delays and did not adversely affect oncologic outcomes such as rate of optimal tumor debulking and progression-free survival (table

S1). The median overall survival for the study population was 49.6 months (30.1 months) (Fig. 1A). Inhibition of IDO1 enzyme activity in plasma and ascites was assessed by measuring Trp and Kyn (table S3). Compared to baseline, plasma Trp increased slightly in 10 of 12 (83%) patients, and plasma Kyn and Kyn:Trp ratio decreased by day 15 (D15) in 9 of 12 (75%) patients (fig. S1, B to D). Paired ascites, as a surrogate for the TME (fig. S2), exhibited a similar trend (fig. S1, E to G).

Plasma EPA concentration was measured to assess drug exposure-response relationships with respect to Trp and Kyn. A prior population pharmacokinetic/pharmacodynamic (PK/PD) model (19) was used with sparse individual EPA and Kyn concentrations to compute individual estimates and link EPA concentration to inhibition of IDO1-mediated Trp → Kyn bioconversion (figs. S1, H and I, and S3). Simulated PK/PD profiles compared against observed data in a representative subject (fig. S1J and table S4) demonstrated typical PK/PD steady-state behavior for drug concentrations and effects. In addition, the model recapitulated central tendencies and variability in observed EPA exposure and response for the study population (fig. S1, K to M). There was no apparent correlation between net exposure [average steady-state EPA concentration ( $C_{ss}$ )] and maximum percent change in Kyn from baseline, suggesting that variability in drug exposure is not associated with PD variability. Overall, PK/PD modeling indicates that 600 mg twice per day achieves sufficient and optimal plasma concentrations for inhibiting IDO1-mediated Trp → Kyn bioconversion.

### Metabolomic analyses uncovers alternative pathways of Trp catabolism upon blockade of Kyn pathway

We hypothesized that IDO1 blockade may affect the metabolic fate of Trp and its downstream catabolites. Therefore, we interrogated paired pre- and posttreatment plasma and tumor for key metabolites along the Kyn, serotonin, nicotinamide (Nic), tricarboxylic acid (TCA), and purine/pyrimidine metabolism pathways (fig. S4A). Unsupervised principal components analysis (PCA) and supervised partial least squares discriminant analysis (PLSDA) of intratumoral metabolomic profiles showed almost complete separation of D00 versus D15 samples, suggesting that blockade of IDO1 changed the metabolic profile of the TME (Fig. 1B and fig. S4B). Alongside expected reductions in Kyn pathway metabolites, we observed intratumoral accumulation of metabolites within the Nic, TCA, and purine/pyrimidine pathways (Fig. 1C). Of the key metabolites contributing to this unique TME profile, D15 reduction in kynurenic acid (KA) was also accompanied by elevation of glutamate and aspartic acid (fig. S4C). Moreover, amounts of some key metabolites within the Nic/NAD<sup>+</sup> pathway [including quinolinic acid (QA) and Nmethylnicotinamide], the TCA cycle, and purines/pyrimidines were increased in tumor at D15 (Fig. 1C and fig. S4A). To assess the impact of changes in each metabolite on the pathway structure, metabolite pathway enrichment and pathway topological analysis based on betweenness centrality (Fig. 1D) showed that the overall effect was especially prominent for the Kyn pathway and for Nic, TCA, and purine/pyrimidine generation. Together, inhibition of IDO1 by EPA efficiently blocked the Kyn pathway but resulted in elevation of serotonin and Nic/NAD<sup>+</sup> generation.

### Transcriptional signature of IDO1 blockade results in reduced Kyn pathway genes and increased serotonin/Nic pathway genes

Similar to the metabolomic analysis, a survey of the intratumor transcriptional landscape revealed that pre- and post-EPA samples group separately (Fig. 2A), including hierarchical clustering of 511

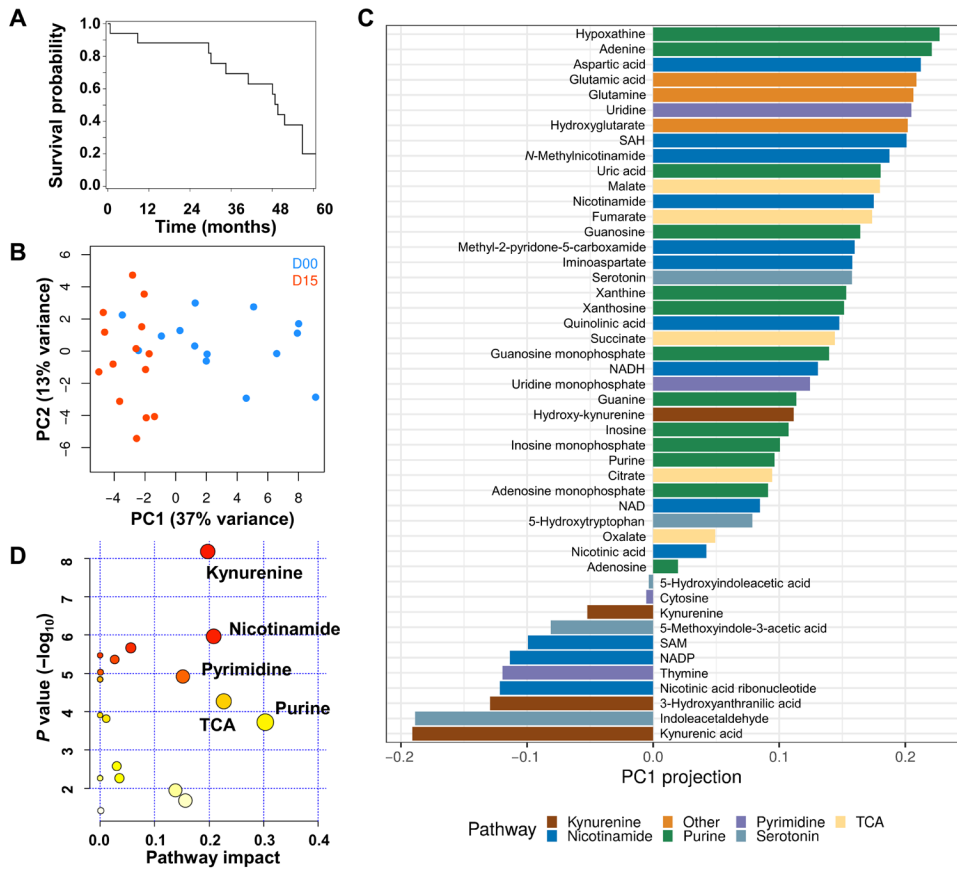


**Fig. 1. Overall survival and metabolic assessment of pre- and posttreatment tumors from patients with ovarian cancer.** (A) Kaplan-Meier summary of overall survival proportions. (B) Unsupervised principal components (PC) analysis of metabolites within tumors from D00 to D15 was performed on tumors from 12 patients. (C) Alterations from D00 to D15 of key metabolite classes relative to Trp abundance based on PC1 projection for the same tumors from the same patients. (D) Pathway impact of changes in metabolite classes.

down-regulated and 697 up-regulated genes (Fig. 2B). Functional enrichment analyses of differentially expressed genes (DEGs) revealed three main pathways: major histocompatibility complex (MHC) class I antigen processing and presentation, Notch/phosphatidylinositol 3-kinase, and chromatin modifiers (fig. S5, A and B). A net reduction in expression of genes along the Trp catabolism pathway was observed from D00 to D15 (Fig. 2, C and D), confirming the transcriptional impact of IDO1 blockade. No change in IDO2 or TDO gene expression was observed upon EPA treatment; however, down-regulation of kynurenine monooxygenase and kynureninase was observed, indicating that additional downstream enzymatic steps along Kyn generation are also altered by IDO1 blockade and contribute to the altered TME metabolic profile. There was up-regulation of arylformamidase, the enzyme that catalyzes the second step of Trp conversion, probably in response to inhibition of Kyn generation. Quinolinate phosphoribosyltransferase, the enzyme responsible for catabolizing QA to nicotinic acid (NA) mono-nucleotide (NAMN), and NAD<sup>+</sup> kinase, the enzyme that generates NAD phosphate, were also up-regulated, possibly in response to low amounts of QA for de novo NAD<sup>+</sup> synthesis. Except for mono-amino oxidase A (MAOA), expression of numerous genes downstream of serotonin metabolism, such as aldehyde dehydrogenase (ALDH)1B1, ALDH7A1, and amine oxidase copper containing 1 (AOC1),

were also up-regulated, suggesting increased activation of the serotonin pathway (Fig. 2D). Alterations in Trp catabolism pathway were accompanied by an increase in net enrichment of interferon- $\alpha/\beta$  (IFN- $\alpha/\beta$ ) pathway genes (Fig. 2E and fig. S5C). Whereas this was expected to promote tumor immunogenicity, additional analyses revealed concomitant up-regulation of pathways related to MYC targets, transforming growth factor- $\beta$  (TGF $\beta$ ), and Wnt/ $\beta$ -catenin pathways that are likely to be detrimental for antitumor immunity (Fig. 2F) (20–22). We also classified pre- and posttreatment samples into “differentiated,” “immunoreactive,” “mesenchymal,” and “proliferative” molecular subtypes using previously described gene signatures (23) and showed 50% of pretreatment samples to be immunoreactive, with posttreatment samples shifting phenotype to be more differentiated and mesenchymal (table S5). Changes in immune-related genes by RNA sequencing (RNA-seq) were validated by NanoString (fig. S5, D and E). Together, the transcriptomic changes in the TME suggest that EPA treatment not only reduces the expression of genes involved in Trp catabolism along the Kyn pathway but also increased expression of serotonin pathway genes and genes involved in the secondary pathways of Nic/NAD<sup>+</sup> synthesis.

### Integrated analyses of changes in catabolites and transcriptome in the TME confirm secondary pathways of NAD<sup>+</sup> generation upon blockade of Kyn pathway

To investigate the degree of interaction between metabolites and gene expression, we integrated metabolic and transcriptomic datasets to construct a network of changes from D00 to D15 mapped along the Trp, serotonin, and Nic pathways (Fig. 3A). The integrated network analysis revealed two main paths after IDO1 blockade. The first path along the Kyn pathway is upstream of Nic metabolism. The second but less predominant path was along serotonin/melatonin metabolism, in which IDO1 inhibition blocks serotonin catabolism and results in increasing serotonin and 5-OH-Trp accumulation. To determine the strength of the biological relationships between metabolomic and gene expression changes, a correlation network of genes and metabolites was built using Pearson correlation coefficient and partitioned by a graph-clustering algorithm (24). Four clusters were identified (Fig. 3B), associated with Kyn, serotonin, MAOA, or Nic. The membership of genes and metabolites is consistent with their topological relationship in the metabolic network (Fig. 3A). This consistency suggests that each path acts as a coherent component and reflects the different aspects of IDO1 blockade.

The network construction revealed an unexpected elevation in Nic and NAD<sup>+</sup> upon IDO1 blockade (Fig. 3A) alongside increased

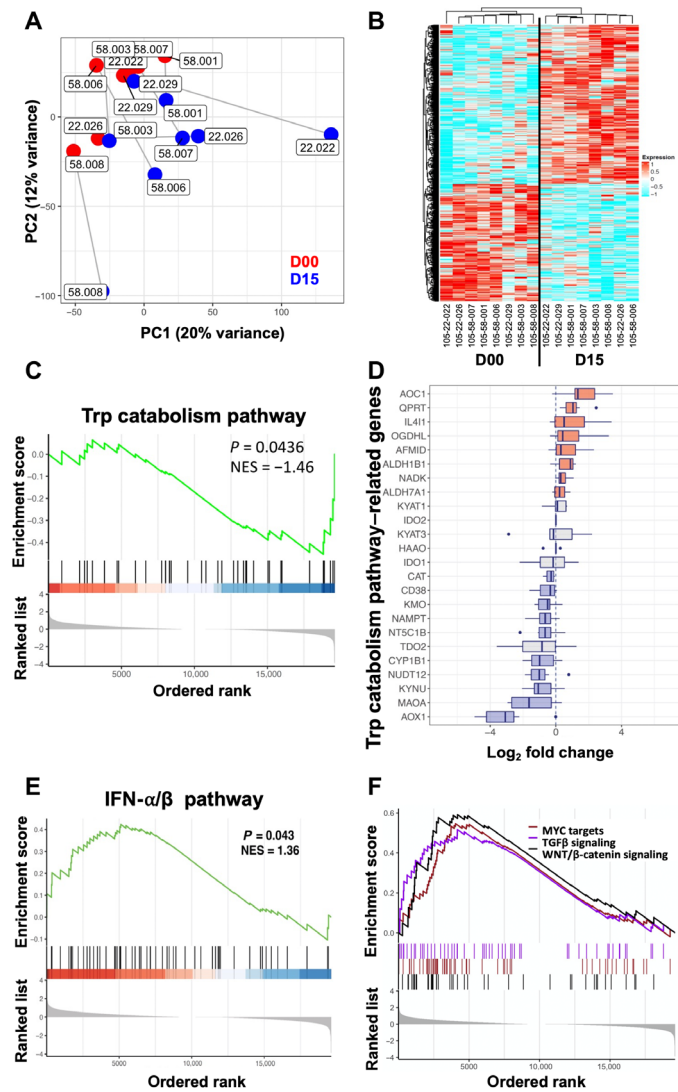


**Fig. 2. Transcriptional immune signature driven by EPA.** (A) Principal components analysis using D00 (red) and D15 (blue) tumors from 12 patients with sufficient amount of paired tissue samples. Matched D00 and D15 samples are connected, indicating the overall shift of the transcriptional pattern within the same patient. (B) Heatmap showing differentially expressed genes [ $n = 1208$ ,  $FDR \leq 0.01$ ,  $\log_2$  fold change (FC)  $\geq 0.5$ ] between D00 and D15. Red and cyan indicate high and low expression, respectively. (C) Gene set enrichment analysis (GSEA) for Trp pathway. Rank statistics (bottom; see y axis) and normalized enrichment scores (top; see y axis) indicate down- and up-regulation, respectively, for the Trp pathway. (D) Boxplot indicating the transcript  $\log_2$  fold changes (x axis) of Trp catabolism. (E) GSEA for IFN pathway. Rank statistics (bottom; see the y axis) and normalized enrichment scores (top; see the y axis) indicate down- and up-regulation, respectively, for the IFN pathway. (F) GSEA plot of pathways up-regulated in D15 versus D00. MYC targets, normalized enrichment score (NES) = 1.72,  $P = 4 \times 10^{-4}$ ; TGF $\beta$  signaling, NES = 1.61,  $P = 5 \times 10^{-3}$ ; WNT/ $\beta$ -catenin signaling, NES = 1.77,  $P = 7 \times 10^{-4}$ .

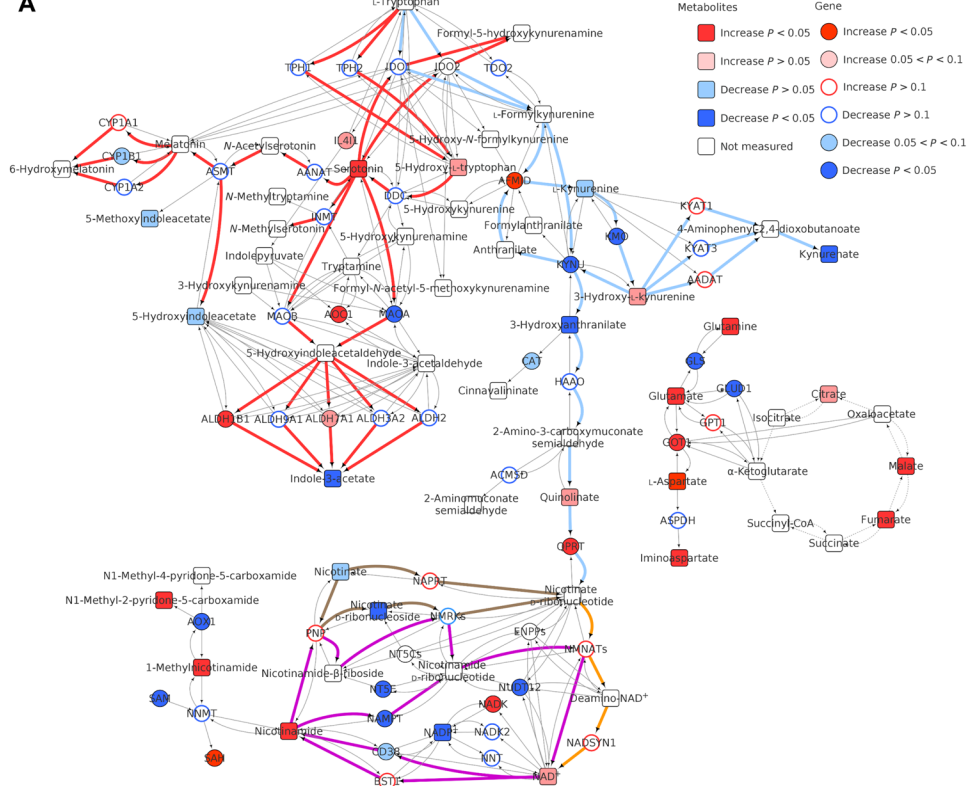
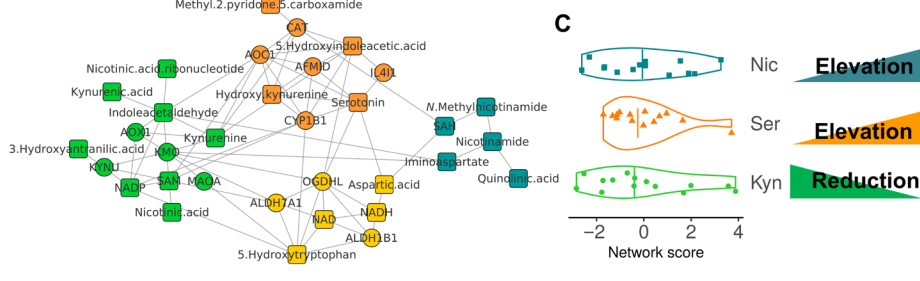
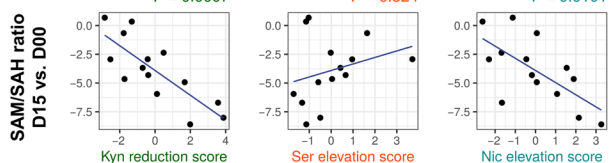
glutamine and glutamic acid (fig. S4A), consistent with previous reports of Trp depletion inhibiting glycolysis and glutaminolysis (25). Efficient reversal of IDO1 activity by EPA reroutes glutamine metabolism and initiates a switch toward a persistent TCA cycle, which could drive the generation of L-aspartate from oxaloacetate and subsequently increased the generation of QA and de novo NAD $^+$

synthesis (Fig. 3A). Consistent with increased de novo generation of NAD $^+$ , we observed elevation in expression of nicotinamide mononucleotide (NMN) adenyllyl transferases (NMNAT) on D15. In addition, we observed elevation of the Preiss-Handler pathway as evidenced by up-regulation of nicotinate phosphoribosyltransferase (NAPRT), which converts NA into NAMN, thereby converging with the de novo pathway of NAD $^+$  synthesis. Last, there was up-regulation of NAD $^+$  synthase (NADS) to catalyze the last step in NAD $^+$  biosynthesis via adenosine triphosphate (ATP)-dependent amidation using glutamine as a donor (26). Nicotinamide phosphoribosyltransferase (NAMPT), a key enzyme in the salvage pathway of NAD $^+$  generation, was down-regulated, suggesting limited contribution by this pathway to the total NAD $^+$  pool.

To better delineate metabolic changes in response to EPA, we defined a quantitative reduction score for the Kyn pathway and an elevation score for the Nic and serotonin pathways. The pathway scores were defined by integrating the change of all metabolites in a cluster and calculated a single measure of overall metabolic activity. Specifically, a higher score for a Kyn cluster generally corresponds to a larger reduction in Kyn at D15, whereas a higher serotonin/Nic score corresponds to a larger elevation in serotonin/Nic. Patients were classified on the basis of these scores (Fig. 3C) to examine the relationship between EPA-driven metabolic changes that could affect antitumor immunity or other tumor characteristics. For example, lower Kyn reduction scores or lower Nic elevation scores are correlated with lower ratios of S-adenosyl methionine (SAM) to S-adenosylhomocysteine (SAH) after EPA treatment (Fig. 3D). This ratio serves as a marker for cellular methylation potential and is predictive of a global hypomethylation state that correlates with cancer aggressiveness (27), pointing to a potential link between EPA-mediated Kyn reduction, Nic elevation, and the epigenetic state of the TME. Although limited pretreatment samples precluded analysis of tumor methylation, posttreatment elevation of 1-methylnicotinamide (1-MNA), a metabolite sink for storing methylation units in cancer cells (Figs. 1B and 3A) (27), supports the possibility of changes in tumor epigenetic state mediated by IDO1 blockade. Collectively, these results indicate that EPA efficiently blocks the major Trp catabolites along the Kyn pathway but subsequently activates alternative NAD $^+$  generation pathways.

### Genome-scale network reconstruction of metabolic subsystem reactions that drive NAD $^+$ generation

Given the concordance of the metabolomic and transcriptomic changes (Fig. 3B), we examined relationships between metabolic genes, their encoded proteins, and reactions they catalyze by mapping data to a human genome-scale metabolic network, Recon3D (28), to explore differential expressions of metabolic reactions in the TME before and after treatment. For each patient, we evaluated all reaction expression scores in the Recon3D metabolic network following the Gene-Protein-Reaction (GPR) mapping rule using D00 and D15 gene expression data. Differential expression scores of metabolic reactions were used to identify up- and down-regulated metabolic subsystems [two-tailed Fisher exact tests, false discovery rate (FDR)  $< 0.1$ ] after EPA treatment (Fig. 4A). Enrichment of up-regulated reactions revealed a metabolic change toward the pentose phosphate pathway (PPP) after EPA treatment (Fig. 4B) in which glucose-6-phosphate is diverted away from glycolysis toward PPP. The resulting phosphoribosyl pyrophosphate (PRPP) metabolite in the PPP subsystem is critical for purine/pyrimidine biosynthesis

**A****B****D**

**Fig. 3. Metabolic assessment of tumors reveals alternative pathways for Trp catabolism.** (A) Integrated transcriptomic and metabolomics network of Trp and nicotinamide (Nic) metabolism in tumors from 12 patients. Major paths of Trp and NAD<sup>+</sup> metabolism are marked: (i) Kyn generation upstream of kynureate production and Nic metabolism (blue lines), (ii) serotonin and melatonin metabolism (red lines), (iii) Preiss-Handler pathway for NAD<sup>+</sup> synthesis (brown), (iv) de novo synthesis pathway for NAD<sup>+</sup> synthesis (purple), and (v) salvage pathway for NAD<sup>+</sup> synthesis and Nic metabolism (orange). (B) Correlation network of genes and metabolites in Trp metabolism and Nic metabolism pathways clustered by greedy maximization of modularity. Four clusters were identified: cluster Kyn, cluster Ser, cluster NAD, and cluster Nic. (C) Kyn reduction, serotonin elevation, and Nic elevation scores from D00 to D15 in samples evaluated by transcriptomics and metabolomics. (D) Linear regression analysis was performed for associations between changes in SAM:SAH ratio, and scores were as follows: Kyn cluster,  $R^2 = 0.63$ ; Nic cluster,  $R^2 = 0.44$ ; and serotonin cluster,  $R^2 = 0.08$ .

and serves as a cosubstrate for NAD<sup>+</sup> synthesis along all three key NAD<sup>+</sup> biosynthetic pathways (Fig. 4C) (29). Subsystem reactions in the de novo and Preiss-Handler pathways were up-regulated upon

EPA treatment, but the salvage pathway was down-regulated, further suggesting a limited contribution of this pathway to NAD<sup>+</sup> biosynthesis upon IDO1 blockade. Downstream reactions for NAD<sup>+</sup> generation were overexpressed, indicating that alterations in the NAD<sup>+</sup> biosynthetic pathway upon EPA treatment results in increased NAD<sup>+</sup> generation. Because PRPP serves an essential substrate in purine/pyrimidine biosynthesis by providing a ribose ring for nucleotide bases (29), elevated PRPP generation is complemented by increased amounts of intermediate molecules using the ribose ring such as adenine, uridine, uric acid, xanthine, and xanthosine (fig. S4, A and C).

Differentially regulated reactions further revealed up-regulation of solute transporters responsible for the flux of citrate/isocitrate across the mitochondria, in exchange for the entry of cytosolic malate (Fig. 4A and table S6) (30). Concentrations of key TCA metabolites and reactions responsible for their generation were increased at D15 (Fig. 4E), indicating a more active TCA cycle. Whereas TCA reactions were increased by IDO1 blockade, pyruvate transport into the mitochondria was down-regulated (Fig. 4, B and E, and table S6). The down-regulation of pyruvate transport triggered a compensatory up-regulation of the malate-aspartate shuttle for maintaining oxidative phosphorylation reactions. Up-regulation of the malate-aspartate shuttle is consistent with the observed increase in glutamate and aspartate with IDO1 blockade (fig. S4, A and C). Last, there was a posttreatment up-regulation of expression of solute carrier family 7 member 5 (SLC7A5), an antiporter of 3-hydroxkynurnine (HKyn) and Trp across cell membranes (31). The redistribution of Trp and HKyn by SLC7A5 overexpression resulted in elevated HKyn normalized to Trp (fig. S4A).

### EPA alters the composition and spatial relationships in the TME

To determine the impact of IDO1 blockade on CD8<sup>+</sup> T cell infiltration and IDO1 expression in the TME, we examined matched baseline and posttreatment biopsies from 13 patients with sufficient specimens by conventional immunohistochemistry (IHC) and imaging mass cytometry (IMC). IHC revealed that EPA treatment was accompanied by increases in absolute frequencies of CD8<sup>+</sup> T cell infiltration in 3 of 13 [23%; 95%

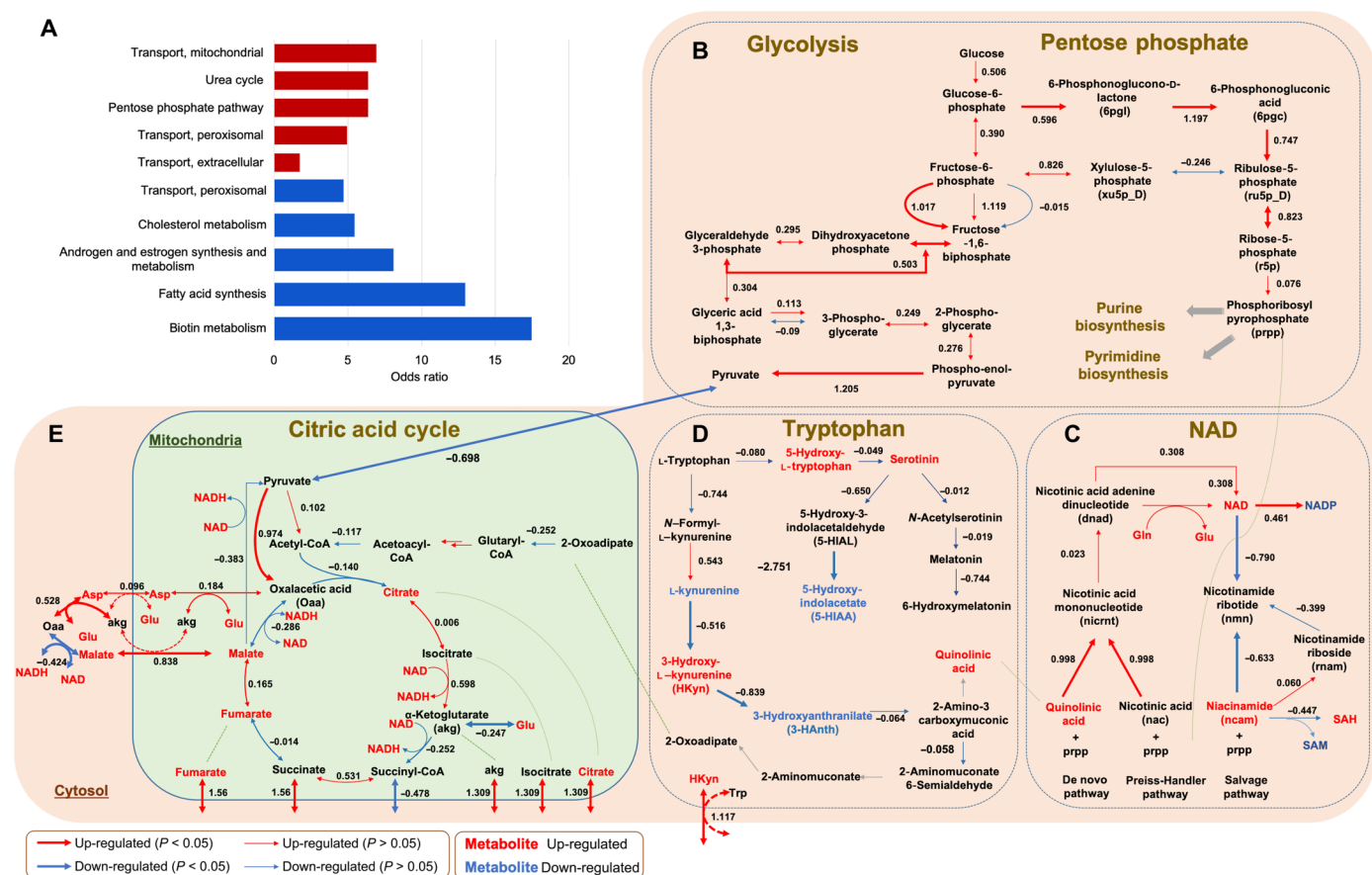


**Fig. 4. Genome-wide reconstruction of metabolic subsystem reactions using reaction differential expression analysis on Recon 3D human metabolic network.** (A) Enrichment analysis of the reaction differential expression in the Recon3D model. Overrepresented metabolic subsystems ( $\text{FDR} < 0.1$ ) are up-regulated (red) or down-regulated (blue). Significantly altered metabolic subsystems of (B) glycolytic and pentose phosphate pathway, (C)  $\text{NAD}^+$  biosynthesis, (D) Trp metabolism, and (E) citric acid cycle. Metabolites are represented as nodes on the network with red indicating up-regulation or blue signifying down-regulation between D00 and D15. Values above reactions are mean log fold change of the reaction expression.

confidence interval (CI), 21 to 31%] patients and increased proportion of  $\text{CD8}^+$  T cells as measured by  $\text{CD8:CD3}$  ratio in 7 of 13 (53%; 90% CI, 42 to 65%) patients (Fig. 5A and fig. S6). However, there was an increase in IDO1 expression from baseline in 8 of 11 (73%; 90% CI, 54 to 85%) patients (Fig. 5B and fig. S7). This finding could be explained by its IFN- $\gamma$ -inducible expression as an adaptive resistance mechanism (32) that could result from  $\text{CD8}^+$ ,  $\text{CD4}^+$ , or NK cells (fig. S5F). Analysis using cytometry by time of flight (CyTOF) revealed an increase in the proportion of  $\text{CD8}^+\text{IFN}\gamma^+$  and  $\text{CD4}^+\text{IFN}\gamma^+$  T cells at D15 ( $P = 2.3 \times 10^{-7}$  and  $P = 0.004$ , respectively), but not NK cells ( $P = 0.09$ ), suggesting that the major source of IFN- $\gamma$  is  $\text{CD8}^+$  T cells and CD4 $^+$  T helper 1 ( $\text{T}_1$ ) cells (fig. S6). It is also possible that increased posttreatment IDO1 expression may represent an adaptive increase in response to higher residual Trp amounts within the TME (fig. S1G). In addition, we noted some exceptions in patients, where increased  $\text{CD8}^+$  TIL was accompanied by decreased IDO1 expression and vice versa (fig. S7, A and B). Because of limited tissue quantity, we used multiplexed IMC for refined evaluation of TME alterations and spatial relationships relative to key cellular and molecular markers.

Expression of nine evaluable markers was captured in multiple 1-mm<sup>2</sup> regions of interest (ROIs) (table S7) to define tumor, stroma,

and immune cells relative to IDO1 expression. We predicted cell boundaries and generated masks for tumor, stroma,  $\text{CD8}$ ,  $\text{FoxP3}$ , and IDO1 $^+$  cells before extracting mean intensity amounts for all markers for downstream analyses (fig. S8, A and B). The change in fraction of  $\text{CD8}^+$ ,  $\text{FoxP3}^+$ , and IDO1 $^+$  cells within the TME (inclusive of tumor and stromal regions) from baseline to post-treatment was consistent with IHC. Alongside an increase in the fraction of  $\text{CD8}^+$  T cells after EPA treatment, tumors exhibited a concomitant increase in IDO1 $^+$  cells and a modest reduction in  $\text{FoxP3}^+$  cells (Fig. 5C and fig. S8B). Because increased human leukocyte antigen - DR isotype (HLA-DR) expression in the TME is known to predict increased inflammation and, when coexpressed with IDO1, can be an indicator of an ensuing IFN-inducible immune response, we evaluated coexpression of HLA-DR and IDO1 in tumor cells. Increased HLA-DR $^+$ IDO1 $^+$  tumor cells after treatment (Fig. 5D) also associated with an increase in activated  $\text{CD8}^+\text{CD27}^+$  T cells within the tumor regions (Fig. 5E). The fine spatial resolution afforded by IMC allowed us to test the hypothesis that EPA treatment would alter the geographical location of immune cells relative to tumor cells. We calculated a distance score capturing the relationship between the total number of IDO1 $^+$ ,  $\text{CD8}^+$ , or  $\text{FoxP3}^+$  cells within 100  $\mu\text{m}$  of tumor cells and their mean Euclidean distance. A

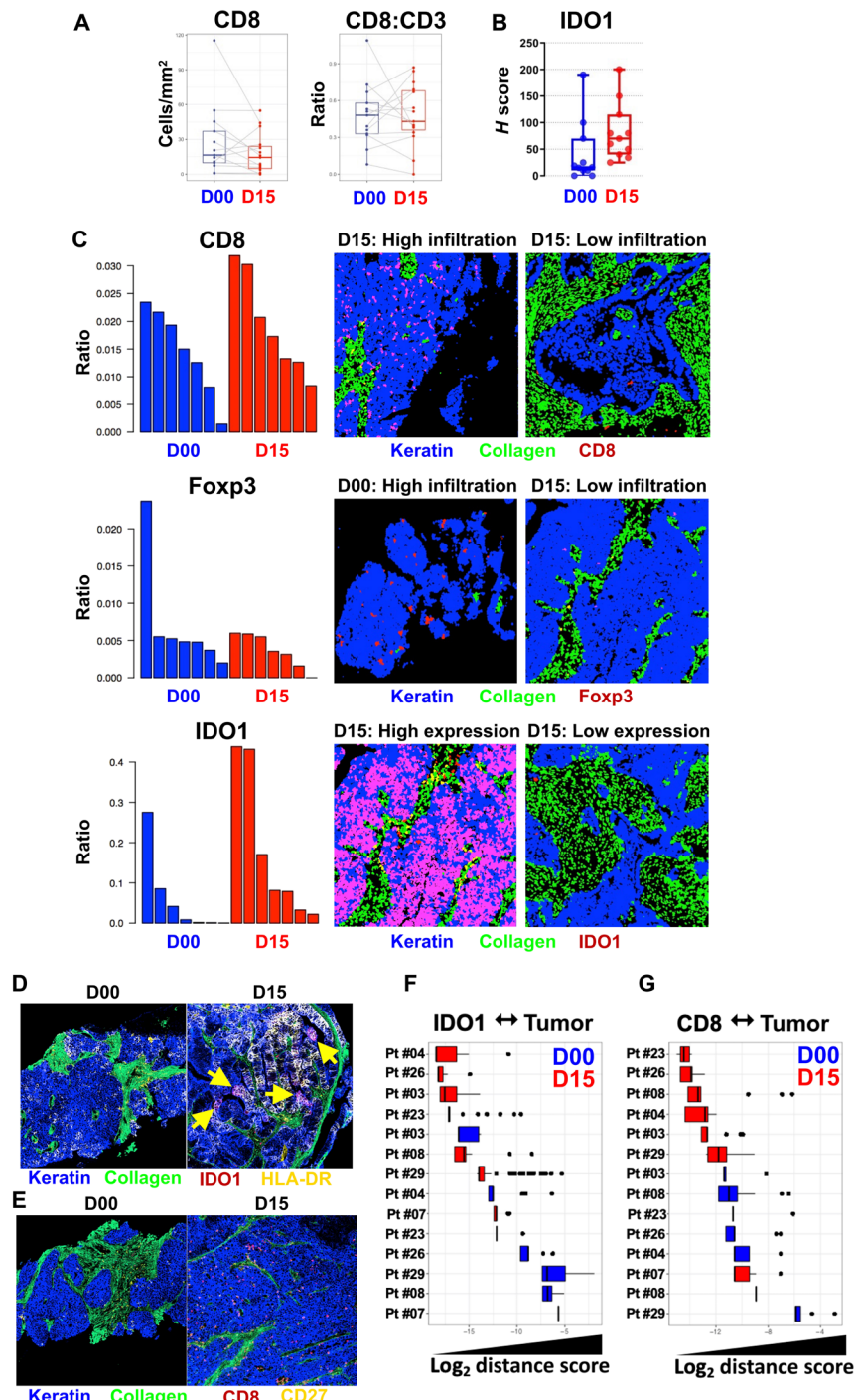


**Fig. 5. Spatial relationship of immune cells within the TME.** (A) IHC measurement of tumor-infiltrating CD3 and CD8 expression at D00 and D15 across 12 patients. (B) IHC measurement of IDO1 expression based on *H* score in D00 and D15 tumor tissue. (C) Quantification of CD8<sup>+</sup>, FoxP3<sup>+</sup>, and IDO1<sup>+</sup> cells from IMC staining. Bar plots (left) indicate the ratio of marker positive cells calculated over the total number of tumor and stroma cells, separated by D00 (blue) and D15 (red). IMC representative mask images of samples with high or low infiltration as indicated by the corresponding bar plots. (D) IMC images highlighting IDO1 and HLA-DR expression and changes between D00 (left) and D15 (right). Yellow arrows indicate focal points of colonization. (E) IMC analyses indicating CD8 and CD27 coexpression in samples at D00 (left) and D15 (right). (F and G) Distance score of IDO1<sup>+</sup> cells (F) and CD8<sup>+</sup> cells (G) versus keratin<sup>+</sup> tumor cells from D00 to D15, ordered by distance to tumor cells. Red and blue indicate samples at D00 and D15, respectively, thus showing separation between the two time points.

lower distance score was observed for IDO1<sup>+</sup> cells relative to tumor cells, indicating a higher number of tumor cells with increased IDO1 expression after EPA treatment (Fig. 5F). Moreover, the distance score of CD8<sup>+</sup> T cells relative to tumor cells also decreased at D15, suggesting the ability of CD8<sup>+</sup> T cells to accumulate at closer proximity to tumor cells upon IDO1 blockade (Fig. 5G). This pattern was not observed for FoxP3<sup>+</sup> cells (fig. S8C).

Next, we examined the relationship between the expression of genes in MYC, Wnt/β-catenin, and TGFβ pathways and the density of infiltrating T cells using parallel IMC data. As expected from Fig. 2F, individual patient changes in MYC, TGFβ, and Wnt/β-catenin pathways showed up-regulation in most patients, but either no change or down-regulation in others (fig. S9A). We illustrate the impact of up-regulation of TGFβ and Wnt/β-catenin pathways on T cell infiltration in patient #003, showing reduction in CD3/CD8/granzyme B and CD3/CD8/CD27 cells by IMC on D15 (fig. S9B). In contrast, patient #008 exhibited a decrease in the TGFβ pathway and, to a lesser extent, in the Wnt/β-catenin pathway, which was accompanied by up-regulation in CD3/CD8/granzyme B and CD3/CD8/CD27 cells at D15 (fig. S9B).

### Functional attributes of immune cell populations grouped by metabolic clusters of the TME after IDO blockade

We next assessed the phenotype and functional fate of immune populations infiltrating the TME by CyTOF (table S8 and Fig. 6A). We identified 12 main clusters defining cell specificity from D00 and D15 (Fig. 6A). As shown in Fig. 6B, the CyTOF markers were most abundant in the five clusters that define the major immune cell subsets, and there was a net separation between pretreatment and post-treatment tumor samples, indicating alterations in the immune landscape upon IDO1 blockade (Fig. 6, C and E). Consistent with IMC data, after IDO1 blockade, an increased proportion of CD8<sup>+</sup> T cells expressed IFN-γ (fig. S6). There was also increased CD56<sup>+</sup> NK cell accumulation in the TME and blood (Fig. 6, D and E, and fig. S5F), in parallel with increased early growth response protein 1 (Egr1) expression in D15 samples detected via RNA-seq (fig. S5C).

On the basis of the altered profile of immune cells, we next examined whether phenotypic changes from D00 to D15 correlated with the three metabolic clusters as defined in Fig. 3C based on Nic elevation, serotonin elevation, and Kyn reduction. Although EPA treatment did not target a specific antigen, at D15, we observed that Kyn reduction positively correlated

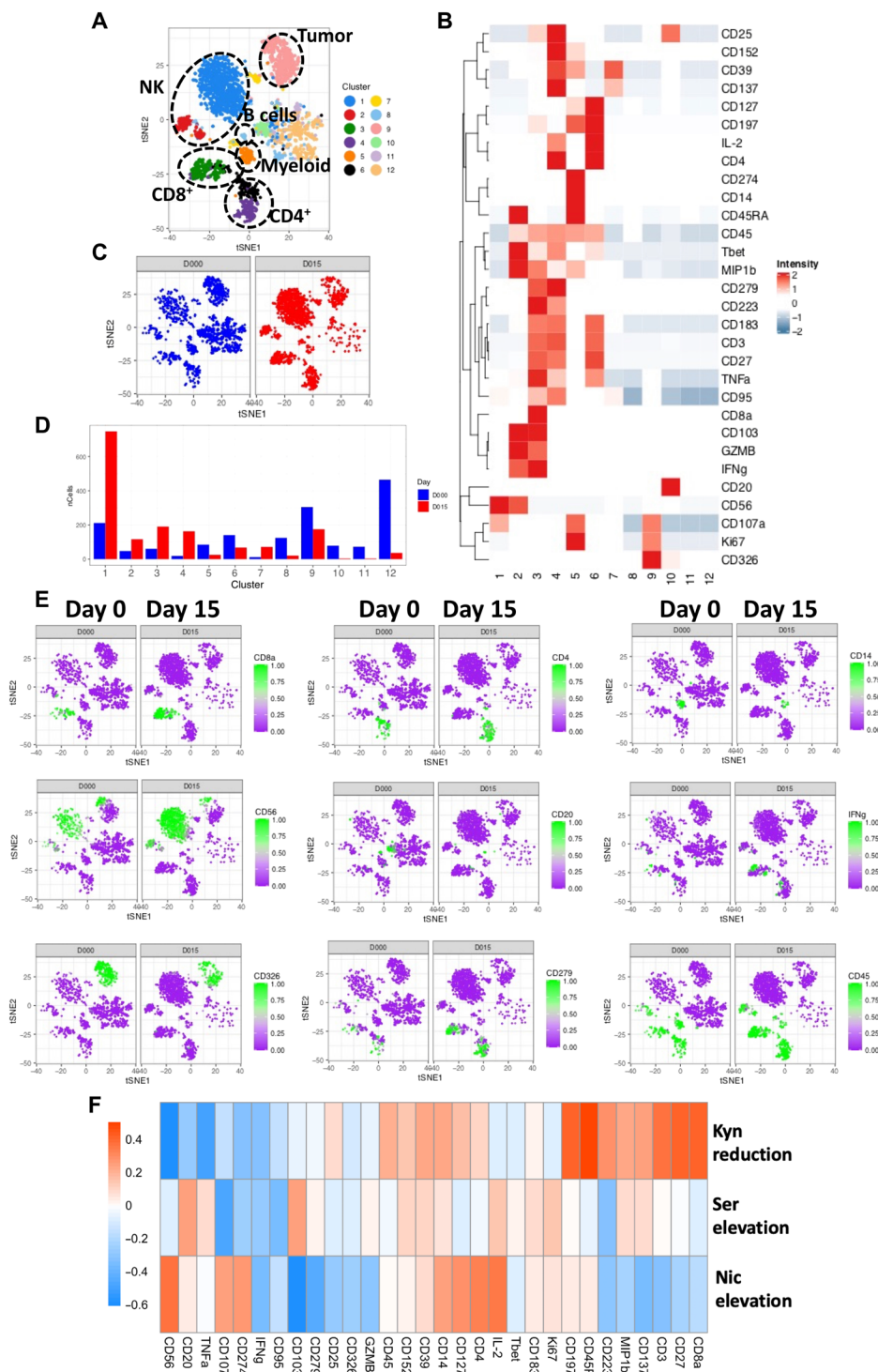


**Fig. 6. Phenotypic and functional attributes of immune cells infiltrating tumors after IDO1 blockade.** CyTOF analysis of samples at D00 and D15 in 13 patients. (A) t-distributed stochastic neighbor embedding (tSNE) projection of the 12 clusters identified highlighting the predominant cell types. (B) Heatmap of the median abundance of the markers used for CyTOF analysis per cluster. Red and blue cells indicate high and low abundance, respectively. (C) tSNE projection of data acquired from single-cell tumor suspension indicating distribution between D00 (blue) and D15 (red). (D) Number of cells per cluster per time point (D00, blue; D15, red). (E) Distribution of key immune markers across clusters, split by days, with green and purple indicating high and low marker abundance, respectively. (F) Correlation of immune marker expression with metabolic scores. Orange and blue indicate positive and negative correlation, respectively.

with the accumulation of CD8<sup>+</sup> lymphocytes expressing CD39 marker associated with tumor-reactive T cells, suggesting that IDO1 blockade may drive tumor-specific T cell infiltration (Fig. 6F) (33). In contrast, serotonin elevation was associated with a reduction in CD25 expression, indicating skewing toward less activated T cells. Nic elevation produced a neutral effect on several markers, but led to a decrease in granzyme B, CD27, and CD137 and an increase in programmed death-ligand 1 (PD-L1) (Fig. 6F).

The key observation of Nic elevation upon IDO1 blockade prompted us to evaluate the impact of key metabolites along these pathways on the functional attributes of T cells. We observed that NAD<sup>+</sup> inhibited CD8<sup>+</sup> T cell proliferation, whereas serotonin did not (fig. S10A). The suppressive effect of NAD<sup>+</sup> prompted us to further evaluate metabolites along the three pathways of NAD<sup>+</sup> synthesis: (i) de novo pathway from Trp to QA; (ii) Preiss-Handler pathway using NA; and (iii) salvage pathway starting from either Nic or nicotinamide riboside (NR), both of which are metabolized to NMN and subsequently to NAD<sup>+</sup>. As shown in fig. S10A, only NAD<sup>+</sup> suppressed T cell proliferation and survival, whereas precursors from all three NAD<sup>+</sup> synthesis pathways did not (fig. S10A). NAD<sup>+</sup> affected the ability of activated CD8<sup>+</sup> T cells and CD4<sup>+</sup> T cells to exert their effector function by reducing the frequency of IFN- $\gamma$ - and interleukin-2 (IL-2)-expressing cells (fig. S10, B and D).

### Targeting the NAD<sup>+</sup> metabolic pathway to enhance the efficacy of IDO blockade in a preclinical ovarian cancer model

To test whether IDO blockade results in elevation of the NAD<sup>+</sup> biosynthetic pathways in a syngeneic murine intraperitoneal orthotopic ovarian cancer model, we used the IE9mp1-mIDO1 cell line that stably expressed the murine IDO1 (mIDO1) gene, where the gene product demonstrated functional enzyme activity as measured by elevated Kyn production (34). Mice were challenged intraperitoneally (ip) with  $1 \times 10^7$  IE9mp1-mIDO1 or IE9mp1-empty-vector tumor cells and treated with EPA (300 mg/kg) by oral gavage, 5 days on and 2 days off, from D07 to D21. Subgroups of these mice were treated with FK866, a small-molecule inhibitor of NAMPT, the enzyme that catalyzes one of the active

pathways of NAD<sup>+</sup> synthesis. FK866 was administered at a dose of 500 µg, ip, once every week for 3 weeks (D13, D20, and D27). Consistent with the human studies, treatment of mice with EPA increased the NAD<sup>+</sup> biosynthetic pathways compared with vehicle, but gene expression analysis indicated that the ability of FK866 to blunt EPA-associated elevation in NAD<sup>+</sup> biosynthetic pathways was not significant (fig. S11B). Moreover, FK866 was insufficient to enhance the therapeutic effect of EPA on tumor progression (fig. S11B), probably attributable to incomplete blockade of NAD<sup>+</sup> generation via additional enzymes including NMNAT, NAPRT, and NADS. As shown in Fig. 1 and fig. S4A, IDO blockade resulted in elevation of downstream metabolites of NAD<sup>+</sup> such as adenosine monophosphate (AMP), inosine, and uric acid in patients, indicating that the observed EPA-mediated NAD<sup>+</sup> elevation also resulted in generation of NAD<sup>+</sup> metabolites that could be ligands for purinergic receptors. Therefore, we tested T cell proliferation in the presence of NAD<sup>+</sup> and blocked individual purinergic receptors in T cells in vitro. The antagonist/receptor pairs that did not recover T cell proliferation suppressed by NAD<sup>+</sup> were (i) oxidized ATP/P2X7, P2Z; (ii) NF449/P2X1; (iii) NF110/P2X3; (iv) PSB36/A1; (v) 5-BDBD/P2X4; and (vi) MRS2279/P2Y4. On the other hand, antagonists against A2a (SCH58261) and A2b (PSB1115) as well as the combination of both A2a and A2b antagonists rescued NAD<sup>+</sup>-mediated suppression of T cell proliferation (Fig. 7A). These findings prompted us to test A2a, A2b, and A2a/A2b receptor blockade in combination with the IDO inhibitor in the IE9mp1-mIDO1 intraperitoneal ovarian model *in vivo* (34). Using the intraperitoneal IE9mp1-mIDO1 model, mice were treated with EPA (300 mg/kg by oral gavage; 5 days on and 2 days off from D7 to D21), with or without A2a, A2b, or A2a/A2b antagonists (1 mg/kg, ip; 5 days on and 2 days off from D7 to D21). The combination of EPA and A2a/A2b receptor blockade significantly increased survival compared to the single- or no-treatment group (56 days versus 37 days; *P* < 0.01) (Fig. 7B) and resulted in a T cell infiltrative immune signature (Fig. 7C). These results confirm our *in vitro* data showing that NAD<sup>+</sup> suppressed T cell function via A2a and A2b purinergic receptors, and the combination of IDO inhibition and A2a/A2b receptor blockade efficiently improved the survival of ovarian tumor-bearing hosts. Together, accumulation of potentially immunosuppressive Kyn metabolites, chiefly NAD<sup>+</sup>, by IDO1 blockade may play a role in the inability of EPA to robustly drive antitumor responses and could potentially be overcome by targeting NAD<sup>+</sup> signaling.

## DISCUSSION

This neoadjuvant window-of-opportunity clinical trial demonstrates that the IDO1 inhibitor, EPA, efficiently blocks the Kyn pathway of Trp catabolism in patients with advanced EOC. PK/PD modeling suggested that the 600-mg twice a day dose achieved sufficient plasma concentrations to inhibit IDO1-mediated Trp → Kyn bioconversion. Simulations of the dose-response relationship confirmed that the 600-mg dose is in the upper maximal effect plateau, which is consistent with clinical observations. Although individual PK/PD profiles were well described by the model, net drug exposure was not correlated with steady-state Kyn amounts. This suggests that variable drug exposure cannot explain the extent of PD variability and necessitates the search for atypical covariates from comprehensive immunologic, transcriptomic, and metabolomic data sources. Changes in Kyn and downstream metabolites were accompanied by an overall increase

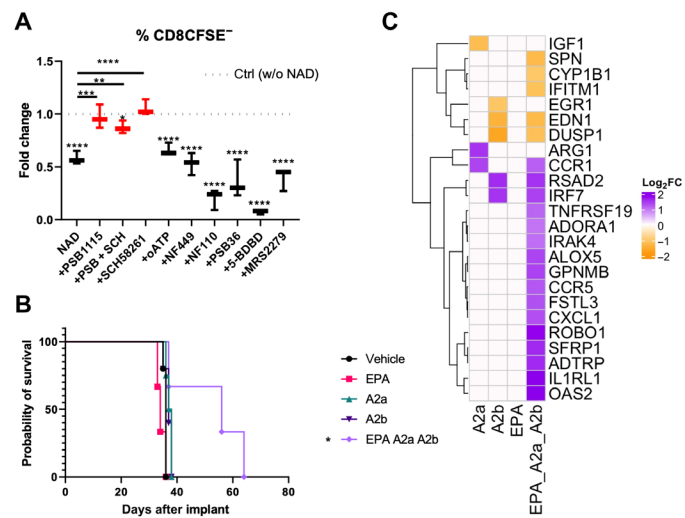


**Fig. 7. Effects of purinergic receptors on NAD<sup>+</sup>-mediated T cell suppression.** (A) Cumulative data of the fold change in human healthy donor CD8<sup>+</sup> T cell proliferation stimulated with anti-CD3/CD28 beads in the presence of the indicated combinations of NAD and antagonists to A2BR (PSB1115), A2AR (SCH58261), P2X (oATP), P2X1R (NF449), P2X3R (NF110), A1R (PSB36), P2X4R (5-BDBD), and P2Y1R (MRS2279). In all box charts, the median and min-max of the values are presented. \**P* < 0.05, \*\**P* < 0.01, \*\*\**P* < 0.001, and \*\*\*\**P* < 0.0001. Wilcoxon and one-way analysis of variance (ANOVA). (B) Survival data of IE9mp1-mIDO1 tumor-bearing mice treated with EPA, A2a, A2b receptor antagonist, or combination of EPA, A2a, and A2b receptor antagonist (*n* = 5 animals per group). Mice were treated by oral gavage with EPA (300 mg/kg) in 200 µl of 0.5% methylcellulose, intraperitoneal injection 5 days on and 2 days off from D7 to D21, with or without (i) NAMPT inhibitor FK866 (500 µg per mouse, i.p.) once every week for 3 weeks (on D13, D20, and D27) and (ii) with or without A2a, A2b, or A2a/A2b antagonists (1 mg/kg, i.p.; 5 days on and 2 days off from D7 to D21). \**P* < 0.05 compared to vehicle. Statistical analysis was calculated using a log-rank analysis. (C) Heatmap representing the log<sub>2</sub>FC of core set genes of immune pathways that are significantly differentially expressed (FDR < 0.05) in the treatment groups compared with the vehicle group of mice. Blue and red indicate down- and up-regulation, respectively.

in the net enrichment of genes in the IFN and MHC class I antigen processing and presentation pathways, along with an increase in the proportion of activated CD8<sup>+</sup> T cells in the TME. The degree of Kyn reduction positively correlated with increases in markers, indicating lineage skewing toward T<sub>H</sub>1, effector T cells, and effector memory T cells. Although there was an overall increase in IDO1 expression, posttreatment CD8<sup>+</sup> TILs were able to reside at a closer distance to IDO1<sup>+</sup> tumor cells, indicating the potential of EPA to increase the opportunity for T cells to efficiently engage tumor targets. Together, these findings indicate that EPA is an effective pharmacologic blocker of the Kyn pathway and is capable of mediating an immune signature in the TME that could be favorable for antitumor immunity. However, our integration of transcriptomic and metabolomic measurements beyond Kyn uncovered evidence of a metabolic adaptation that could constrain the beneficial effects of IDO1 blockade.

The metabolic changes in the TME upon IDO1 blockade by EPA included elevation of serotonin, Nic, NAD<sup>+</sup>, TCA, and purine/pyrimidine metabolism. A possible explanation for the increased synthesis of serotonin in the TME is that inhibition of IDO1 may elevate Trp concentration systemically or locally and shunt catabolism toward the serotonin pathway. However, across 6 studies

of EPA monotherapy and 22 studies of EPA in combination with other agents (a total of 2490 subjects), only four cases of suspected “serotonin syndrome” have been reported (35). Moreover, the effect of EPA on serotonin amounts in the brain extracellular fluid was minimal in rats (35). In the current study, we evaluated the impact of EPA on serotonin in the human TME. Although the potential consequences of elevated serotonin include reduced IFN- $\gamma$  release by CD8 $^{+}$  T cells and expansion of IL-10-secreting CD4 $^{+}$ FoxP3 $^{+}$ T<sub>regs</sub> (36), these were not observed in our study, indicating that elevation in serotonin in the TME was insufficient to mediate these effects.

NAD $^{+}$  plays a central role as a coenzyme in redox reactions by accepting high-energy electrons from glycolytic and TCA intermediates and feeds electrons into complex I of the electron transport chain to drive oxidative phosphorylation. Beyond this role, NAD $^{+}$  serves as a cosubstrate for adenosine diphosphate (ADP)-ribose (ADPR) transferases, poly(ADP-ribose) polymerases, cyclic ADP-ribose synthases, and sirtuins. Because EPA efficiently blocked the Kyn pathway, any reduction in the amount of its downstream catabolite QA could lead to disruption of NAD $^{+}$  homeostasis. To sustain adequate amounts of NAD $^{+}$  for homeostasis, it is critical for NAD $^{+}$  to be replenished through biosynthetic and salvage pathways or decreased degradation. We detected activation of alternative pathways of NAD $^{+}$  generation, resulting in overcompensation by increasing NAD $^{+}$  amounts upon IDO1 blockade. This observation is supported by up-regulated expression of several key enzymes critical for NAD $^{+}$  generation via the de novo and Preiss-Handler pathways.

Using genome-scale metabolic network reconstruction (28), we uncovered multiple metabolic subsystems that ultimately converge on elevating de novo and Preiss-Handler pathway reactions to sustain NAD $^{+}$  amounts in the TME after IDO1 blockade. The first is diversion of glucose-6-phosphate from the glycolytic pathway to the PPP leading to the generation of PRPP crucial for NAD $^{+}$  biosynthesis. The second is the reduction in the degradation reaction of NAD $^{+}$ . Together, differential reaction expressions in the PPP and NAD $^{+}$  biosynthesis network all lead to an overall increased NAD $^{+}$  in the TME after IDO1 blockade. The third is up-regulation of a solute transporter SLC7A5, an antiporter of HKyn and Trp across cell membranes (31). SLC7A5 overexpression, possibly in response to increased intracellular Trp due to IDO1 blockade, enables cells to simultaneously export Trp and import HKyn. Specifically, overexpression of SLC7A5 is expected to increase the ratio of extracellular-to-intracellular Trp and reduce the extracellular-to-intracellular ratio of HKyn, subsequently leading to de novo NAD $^{+}$  synthesis. The final possible path is via aspartate, for which the potential metabolic route is from increased TCA intermediates driven by elevated glutaminolysis (37). This latter path is consistent with posttreatment elevation in the glutamate  $\rightarrow$  aspartate  $\rightarrow$  iminoaspartate  $\rightarrow$  QA  $\rightarrow$  NAD $^{+}$  chain. However, this path is less likely than other possibilities because synthesis of QA from Asp has been demonstrated in some prokaryotes, such as *Escherichia coli* (38), with no conclusive demonstration of this pathway in animals.

Although the extensive metabolic adaptation that occurs in the TME as a consequence of blocking the Kyn pathway may serve to support tumor sustenance of Warburg metabolism, it is detrimental to the functional attributes of CD8 $^{+}$  T cells. The combined results of our immunophenotypic analyses showed that posttreatment NAD $^{+}$  elevation was associated with a decrease in key CD8 $^{+}$  TIL effector molecule expression, indicating reduced functionality of CD8 $^{+}$  TILs. Upon testing the direct impact of excess Kyn metabolites,

NAD $^{+}$  precursors, and NAD $^{+}$  on CD8 $^{+}$  T cells, we confirmed that NAD $^{+}$  had profound detrimental effects on CD8 $^{+}$  T cell proliferation and function. Mechanistically, we demonstrated that NAD $^{+}$  suppressed T cell function via A2a and A2b purinergic receptors, and the combination of IDO inhibition and A2a/A2b receptor blockade efficiently improved survival of ovarian tumor-bearing mice. For CD4 $^{+}$  T cells, NAD $^{+}$  has been shown to promote conversion of T<sub>H</sub>1/IFN- $\gamma$ -producing cells into suppressive regulatory type 1 cells coproducing IL-10 and driving the switch of induced T<sub>regs</sub> into T<sub>H</sub>17/TGF $\beta$ -producing cells (39). Collectively, our results indicate that the adaptive increase in NAD $^{+}$  could be detrimental to the beneficial effects of EPA in relieving IDO1-mediated immunosuppression.

Our observation of up-regulation of pathways such as MYC, TGF $\beta$ , and Wnt/ $\beta$ -catenin, which are also likely detrimental for anti-tumor immunity (20–22), raises the possibility of alternative IDO1 functions when the catalytic activity is blocked. For example, down-regulation of IDO or blockade by the IDO inhibitor 1-methyl-tryptophan has been shown to potentiate TGF $\beta$ 1-induced epithelial-to-mesenchymal transition (40). In addition, we observed that the degree of Nic/NAD $^{+}$  elevation in ovarian tumor tissues of patients correlated with lower SAM:SAH ratio upon EPA treatment, with implications for tumor methylation potential and gene expression (27, 41). Methylation potential is an important metabolic indicator of cellular methylation status, and a decrease in this parameter has been associated with a global hypomethylation state in cells. 1-MNA accumulation, a known sink for storing methylation units in tumor cells (27), suggests that post-EPA treatment tumors may have a limited capacity to recover methylation units, leading to global hypomethylation. Expression of NNMT in ovarian cancer-associated fibroblasts was recently shown to reduce SAM amounts and histone methylation, resulting in widespread tumor stroma gene expression changes (42). Given the clinical and biological significance of aberrant epigenetic plasticity in tumors, it would be important in future studies to determine the impact of the IDO1 pathway on the epigenetic state of ovarian and other solid tumors.

Our collective data point to the need to address the multiple adaptive metabolic pathways that counteract the potential benefit of IDO1 inhibition, especially the previously unknown contribution of the NAD $^{+}$  biosynthetic pathways. First, to ameliorate tumor generation of NAD $^{+}$ , IDO1 inhibition could be combined with effective inhibitors of multiple pathways of NAD $^{+}$  generation. Second, to reduce the flux of glucose through oxidative PPP, IDO1 inhibition may also be combined with the U.S. Food and Drug Administration-approved G6PD inhibitor, 6-aminonicotinamide. This combination would be beneficial in cancers with overexpression of TP53-induced glycolysis and apoptosis regulator or pyruvate kinase M2, where such overexpression, in turn, reduces the generation of PRPP, the cosubstrate for NAD $^{+}$  biosynthesis (43). Third, to limit the impact of excessive NAD $^{+}$  generation on T cells, IDO1 inhibition may be combined with compounds that block the A2a and A2b purinergic receptors as shown in the current study.

We recognize some potential limitations of our present study. The first is the relatively small sample size of the window-of-opportunity clinical trial. The second is our inability to enhance the therapeutic potential of EPA with FK866 in our preclinical model, probably because of inefficient pharmacologic blockade of all the compensatory NAD $^{+}$  biosynthetic pathways. These results prompted us to reason that NAD $^{+}$ -dependent signaling involves degradation of the dinucleotide (44). Moreover, FK866 and other NAMPT inhibitors have

not demonstrated sufficient tumor selectivity to achieve clinical success (45). In this regard, NAD<sup>+</sup> can be degraded to Nic and ADPR by ADP-ribosyltransferase or CD38, and ADPR can be further degraded into AMP and adenosine by CD203a and CD73 (44). Therefore, to limit the impact of excessive NAD<sup>+</sup> generation on T cells, IDO1 inhibition may be combined with compounds that block the A2a and A2b purinergic receptors, as shown in the current study.

In conclusion, we provide a comprehensive analysis of the impact of IDO1 blockade on the TME and new insights into the potential mechanisms for the lack of clinical efficacy of IDO1 blockade. We showed evidence that blockade of IDO1-mediated Trp catabolism triggers an adaptive metabolic response in the TME of ovarian cancer. We postulate that Kyn pathway blockade leads to an initial reduction in de novo NAD<sup>+</sup> synthesis, thereby triggering activation of alternative pathways of NAD<sup>+</sup> generation driven by multiple mechanisms. Our findings provide rationale for exploring additional metabolic nodes for combination treatment of patients, such as concomitant blockade of IDO1 with NAD<sup>+</sup> targeting by blocking A2a/A2b purinergic receptors to overcome the detrimental metabolic changes in the TME.

## MATERIALS AND METHODS

### Study design

The study protocol (CITN-05, NCT02042430) was approved by the Institutional Review Board at Roswell Park Comprehensive Cancer Center and Masonic Cancer Center at the University of Minnesota, and all patients gave written informed consent. This was a single arm, nonrandomized, open-label study of EPA (INCB024360) given for 2 weeks (D01 to D14) in newly diagnosed patients with ovarian cancer, followed by standard tumor debulking surgery. The 2-week time frame designated for receiving EPA before debulking surgery was considered to not pose a survival risk to patients. EPA was supplied by Incyte Corporation (300-mg tablets) and was administered orally at a dose of 600 mg twice daily for 2 weeks (D01 to D14). Although available PK/PD data at the time of study design indicated >80 to 90% inhibition of IDO1 at doses of  $\geq 100$  mg BID, the 600-mg BID dose was chosen because it has been shown to be well tolerated and effective at rapidly normalizing Kyn/Trp ratios (13) and was being used in another ongoing study (NCT01685255) in patients with ovarian cancer (46). Each patient's tumor was biopsied before therapy, and ascites fluid was collected by paracentesis when present. At the time of debulking surgery on D15 (+7 days), posttreatment tumor tissue from the geographic area of the biopsy was harvested, and ascites fluid was collected if present. Plasma samples were collected on D01 and D14 of treatment before dosing, as well as on D15 and D35. The primary end point of the study was to determine the extent to which EPA altered the number of CD8<sup>+</sup> T cells in the TME. Secondary objectives included safety and tolerability, impact of EPA on Kyn/Trp ratios, gene expression of the TME, and the frequency and phenotype of TILs. In addition, we performed post hoc metabolomic analyses to understand the impact of EPA on downstream Trp catabolism beyond Kyn. The study was designed to declare a positive outcome if at least 9 of 12 patients experience an increase in CD8<sup>+</sup>, because this would provide 90% confidence of a true increase due to treatment (lower limit of Wilson score interval  $> 0.50$ ). With a sample size of 12, there is 78% power to detect an increase if the true rate of increase is 80% (lower bound of 90% Wilson score interval  $> 50\%$ ). Patients without adequate

tissue sampling were replaced, leading to total enrollment of 17 patients. Individual participant data that underlie the results reported in this article, after deidentification, are provided in data file S1.

### Population PK/PD modeling

Individual subject PK and PD parameters were generated by computing maximum a posteriori probability (MAP) Bayesian projections using sparse individual data and a prior nonlinear mixed effects PK/PD model of EPA (EPA) in patients with advanced solid malignancies (19). Briefly, EPA PK was characterized by a two-compartment model with linear elimination in the central compartment and first-order absorption with a fixed lag time ( $T_{lag}$ ) of 0.1 hours

$$\begin{aligned} \frac{d\text{Abs}}{dt} &= -k_a \cdot \text{Abs} \quad \text{Abs}(0) = \text{Dose} \\ \frac{dA_C}{dt} &= k_a \cdot \text{Abs} - \frac{\text{CL} + \text{CL}_D}{V_C} \cdot A_C + \frac{\text{CL}_D}{V_T} \cdot A_T \quad A_C(0) = 0 \\ \frac{dA_T}{dt} &= \frac{\text{CL}_D}{V_C} \cdot A_C - \frac{\text{CL}_D}{V_T} \cdot A_T \quad A_T(0) = 0 \end{aligned}$$

with Abs,  $A_C$ , and  $A_T$  representing the amount of drug in the absorption, central, and peripheral compartments.  $k_a$  is the first-order absorption rate constant, CL and  $\text{CL}_D$  are systemic and distributional clearances,  $V_C$  and  $V_T$  are central and peripheral volumes, and the plasma concentration of EPA ( $C_p$ ) =  $A_C/V_C$ .

The effect of body weight (BW) on apparent [normalized by bioavailability ( $F$ )] clearance ( $\text{CL}/F$ ) and central volume ( $V_C/F$ ) was incorporated, using a power function centered on the median body weight of the population

$$\text{TV}(\theta_j) = \theta_j \cdot \left( \frac{\text{BW}_i}{\text{BW}_{\text{median}}} \right)^b$$

where TV stands for typical value;  $\theta_j$  is  $\theta_{\text{CL}/F}$  or  $\theta_{V_C/F}$ , representing reference values for apparent clearance and volume when  $BW = BW_{\text{median}}$ ; and  $b$  is the classical allometric exponent fixed to 0.75 and 1 for  $\text{CL}/F$  and  $V_C/F$ .

EPA plasma concentration ( $C_p$ ) is linked to the inhibition (INH) of the bioconversion of Trp to Kyn

$$\begin{aligned} \frac{d\text{KYN}}{dt} &= \text{TRP} \cdot (k_1 - \text{INH} \cdot k_1 + k_2) - \text{KYN} \cdot k_{\text{deg}} \\ \text{KYN}(0) &= \text{TRP} \cdot \frac{k_1 + k_2}{k_{\text{deg}}} \end{aligned}$$

with  $k_1$  and  $k_2$  as first-order rate constants for KYN formation via IDO1 and TDO, and  $k_{\text{deg}}$  is the first-order Kyn degradation rate constant. The inhibition function is defined as  $\text{INH} = C_p^\gamma / (\text{IC}_{50}^\gamma + C_p^\gamma)$ , where  $\text{IC}_{50}$  is the EPA concentration producing 50% inhibition and  $\gamma$  is the Hill coefficient. Apparent increase in the sensitivity to the drug after multiple dosing was integrated by allowing different  $\text{IC}_{50}$  values on D01 and D15.

Between-subject variability (BSV) was allowed on all model parameters, except for peripheral volume,  $k_2$ , and  $\text{IC}_{50}$ . BSV was modeled using exponential function, assuming that a parameter ( $P_i$ ) follows a log-normal distribution

$$P_i = \text{TVP} \cdot e^{n_i}, n_i \sim N(0, \omega^2)$$

where TVP is the typical population value of the parameter, and  $n_i$  is a symmetrically distributed, random variable, with a mean of zero

and variance  $\omega^2$ . Residual variability was characterized by the exponential error model for PK and the proportional error model for PD.

Because of sparseness of data, the individual Bayesian estimates were obtained by assuming that they are conditional on the model parameter values in the original model (table S4) (19). Nonlinear mixed effects modeling was done in NONMEM (version 7.2; ICON Development Solutions, Hanover, MD, USA) using the first-order conditional estimation method with interaction, with MAXEVALS set to 0, which enabled the generation of individual subject estimates using a Bayesian algorithm. MAP estimates were obtained by minimizing the objective function

$$O(\vec{n}_i) = -2\text{LL}(\vec{n}_i) = \sum_j \left[ \log \sigma_{ij}^{-2} + \frac{(Y_{ij} - F_{ij})^2}{\sigma_{ij}^{-2}} \right] + \vec{n}_i^T \Omega^{-1} \vec{n}_i$$

with  $Y_{ij}$  and  $F_{ij}$  representing the observation and model solution for the  $j$ th observation of the  $i$ th individual, and  $\text{LL}(\vec{n}_i)$  is the log-likelihood.  $\Omega$  is the covariance matrix of BSV, and  $\sigma$  is the covariance matrix of residual random variability.

Individual subject parameters were used to calculate individual net drug exposures such as average steady-state CP or  $C_{ss}$  and to simulate net drug response (area under the effect curve over one 12-hour dosing period or  $\text{AUEC}_{ss}$ )

$$\begin{aligned} \text{AUC}_{ss(i)} &= \frac{\text{Dose}}{\left(\frac{\text{CL}}{F}\right)_i} \\ \text{AUEC}_{ss(i)} &= \sum_{j=0}^{\tau} \frac{(\text{Base}_i - C_j) + (\text{Base}_i - C_{j+1})}{2} \cdot (t_{j+1} - t_j) \\ C_{ss(i)} &= \frac{\text{AUC}_{ss(i)}}{\tau} \end{aligned}$$

with Base representing the individual subject KYN baseline, which is assumed to be constant;  $i$  represents the dosing interval, and  $j$  is time since dosing at steady state.

### Metabolomic analysis of Kyn, serotonin, and Nic pathways of Trp degradation by liquid chromatography-mass spectrometry

We examined changes in downstream catabolites of Trp including 5-hydroxytryptophan, Kyn, KA, HKyn, 3-hydroxyanthranilic acid (HAA), QA, Nic, NA ribonucleotide, indoleacetaldehyde, 5-methoxyindole-3-acetic acid, iminoaspartate, methyl-2-pyridone-5-carboxamide, serotonin, *N*-methylnicotinamide, and 5-hydroxyindoleacetic acid. In addition, we measured key metabolites in TCA and purine/pyrimidine metabolism because of the role of NAD<sup>+</sup> in driving multiple key steps in these pathways. Tissue samples were stored at -80°C until metabolic extraction.

### PCA, PLSDA, VIP, and pathway topological analysis based on betweenness centrality

The metabolite data were normalized by Trp amounts to have zero mean and unit variance before PCA, to avoid domination of the PCA results by variables with large variance in the original data scale. No missing data were present in the panel of metabolites measured. The data were visualized on the first two components. The projection of each metabolite on the first component, which separates the data of two time points, was visualized using bar plots. PLSDA and VIP (variable importance in projection) were performed

using the online tool available at [www.metaboanalyst.ca](http://www.metaboanalyst.ca) (47). The RNA-seq data used for PCA were initially normalized using DESeq2 and log-transformed. PCA was run on the top 1000 most variable genes. The absolute loadings for the first three principal components can be seen below, showing the weight of each indicated gene in calculating the corresponding principal component.

Pathway topological analysis based on betweenness centrality was used to show that not only are the metabolites with change enriched in the pathways noted, but the changes are also expected to have large impacts on the other metabolites in the metabolic network. The impact scores represent the importance of the metabolites in the metabolic network. They were calculated on the basis of the centrality measures of a metabolite in a given metabolic network. Centrality is a local quantitative measure of the position of a node relative to the other nodes and is often used to estimate a node's relative importance or role in network organization. Specifically, we used relative betweenness centrality to calculate compound importance. The pathway impact is calculated as the sum of the importance measures of the matched metabolites normalized by the sum of the importance measures of all metabolites in each pathway (48).

### Correlation network of genes and metabolites

The networks of Trp metabolism pathway and Nic and NA metabolism pathway were obtained from the Kyoto Encyclopedia of Genes and Genomes (KEGG) database (49) and extracted using the graphite package (50). The two networks were combined by taking the union of the nodes and edges. To identify functional groups of genes and metabolites that are co-regulated, a correlation network was constructed for both metabolites and genes (RNA-seq) in Trp and Nic metabolism pathways. For both transcription and metabolite amount, the differences between D15 and D00 were calculated. The metabolites were also normalized by Trp amounts. The genes were first screened by differential expression analysis between D15 and D00. Only genes with  $P < 0.1$  were selected for correlation network construction because these genes are more likely to be regulated at transcription amounts under EPA treatment.

### Reaction differential expression and enrichment analysis using Recon3D human genome-scale metabolic network

We implemented GPR mapping using the gene expression data and evaluated reaction expression scores for all reactions in the Recon3D human genome-scale metabolic network (28, 31). The first step of the GPR mapping involves computing the protein/enzyme expression score. Multiple genes can be mapped to a single reaction, and single genes could be mapped to multiple reactions. When an enzyme is encoded by a single gene, the enzyme expression score is set equal to the gene expression (log-normalized RNA count). When an enzyme has multiple subunits that are encoded by distinct genes, its expression score is taken to be the minimum expression among the genes. In the last step, we set the expression score of a reaction equal to the enzyme expression score when the reaction is catalyzed by one enzyme or to the maximum enzyme expression scores among isozymes catalyzing the reaction (51, 52). The GPR mapping was implemented in MATLAB (R2018a) using the COBRA toolbox (53). After the GPR procedure outlined above, the log-normalized RNA counts of 19,641 genes from eight patients before and after EPA treatment were mapped to the human Recon3D metabolic network. We used paired *t* tests to calculate the two-sided *P* values of the reaction expression difference between D00 and D15. We identified

differentially expressed reactions using a two-sided *P* value of <0.05 cutoff. Differentially expressed reactions with positive and negative average log FC were labeled as up-regulated (down-regulated). We performed two-tailed Fisher exact tests to identify metabolic subsystems in human Recon3D (28) that are enriched in the set of up-regulated and down-regulated reactions (FDR < 0.1).

### IMC acquisition and analysis

To assess the spatial distribution of immune cell populations, IMC (Hyperion, Fluidigm) (54) was used to analyze pre- and posttreatment tumor sections. Image acquisition after daily tuning was carried out following the manufacturer's instruction at a laser frequency of 200 Hz. Multiple 1-mm<sup>2</sup> ROIs from D00 and D15 were analyzed from each patient for expression of nine evaluable markers. The marker expression intensity associated with individual ROI was used as input for further analysis.

### CyTOF data processing and analysis

The short-term signal fluctuations of Helios were normalized using a bead-based passport P13H2302 (CyTOF version 6.7) to EQ Four Element Calibration bead signals, and viable singletons were gated and exported in Cytobank. The exported files were imported in R (55) using the Bioconductor flowCore package (56) and were normalized (archsin with factor 5) before clustering and differential abundance analysis. Differential abundance between D00 and D15 was calculated using the mean expression of the marker per patient and comparing the two time points with Student's *t* test at *P* = 0.05.

### Assessment of effect of Kyn metabolites, serotonin, NAD precursors, NAD<sup>+</sup>, and purinergic receptor blockade on T cell proliferation and function

Trp and Trp metabolites Kyn, HKyn, HAA, QA, KA, picolinic acid, anthranilic acid, serotonin, NAD<sup>+</sup>, and NAD<sup>+</sup> precursors Nic, NR, NMN, and NA were purchased from Sigma-Aldrich. Healthy donor peripheral blood mononuclear cells ( $1 \times 10^6$ ) were stimulated with anti-CD3/CD28 Dynabeads (Gibco) in the presence of various amounts of the different metabolites in complete medium (RPMI-1640 with 10% fetal bovine serum and 10 U of IL-2) for 3 to 6 days. Normal donor CD8<sup>+</sup> T cells were also cultured with NAD<sup>+</sup> in the presence of different antagonists against purinergic receptors.

### Animal studies

Female and male WT C57BL/6 mice were purchased from the Jackson Laboratory (Bar Harbor, ME), and all animal experiments were carried out according to protocol guidelines approved by the Institute Animal Care and Use Committee (IACUC) at the Roswell Park Comprehensive Cancer Center. The mIDO1 gene or empty vector was retrovirally transduced into mouse ovarian surface epithelial cell line IE9mp1 (34). All cell lines were cultured in complete culture medium: RPMI 1640 (Corning cellgro) supplemented with 10% fetal bovine serum (VWR), 1% sodium pyruvate (100 mM), 1% L-glutamine (200 mM), 1% minimum essential medium non-essential amino acid (100×), 1% penicillin/streptomycin (100×), 2.5% Hepes, and 0.1% β-2-mercaptoethanol (50 mM) in an incubator at 37°C and 5% CO<sub>2</sub>. C57BL/6 mice were challenged intraperitoneally with  $1 \times 10^7$  IE9mp1-mIDO1 or IE9mp1-empty-vector tumor cells in a final volume of 500 μl of Dulbecco's phosphate-buffered saline (Corning cellgro) and treated by oral gavage with IDO1 inhibitor

INCB023843 (300 mg/kg) (Incyte Corp.) in 200 μl of 0.5% methylcellulose, intraperitoneal injection for 5 days on and 2 days off from D7 to D21, with or without (i) NAMPT inhibitor FK866 (Sigma-Aldrich; 500 μg per mouse, i.p.) once every week for 3 weeks (on D13, D20, and D27) and (ii) purinergic receptor A2a or A2b antagonists (SCH58261 from Sigma-Aldrich or PSB1115 from Tocris Bioscience; 1 mg/kg, i.p. 5 days on and 2 days off from D7 to D21). Tumor progression was monitored by measuring abdominal distension to track the accumulation of peritoneal ascites formation. Mice were euthanized by CO<sub>2</sub> asphyxiation and/or cervical dislocation when the abdominal circumference of intraperitoneal tumors reached a 50% girth increase and/or upon detection of declining health conditions as described in our standard operating procedure for body scoring, according to IACUC guidelines.

### Statistics

To elucidate TME changes after EPA treatment, we performed extensive correlative analyses. Differences of means between two groups (pre- and posttreatment time points) were investigated by two-sided Student's *t* tests or partially paired *t* tests as appropriate. Correlations between continuous variables were examined by Pearson correlation or linear regression models with *F* tests. The estimated correlation or regression coefficients, 95% CIs, and *R*<sup>2</sup> are presented in the Supplemental Materials. All tests are two-sided, with corresponding *P* values reported. For comparison of metabolites between time points, both unadjusted *P* values and FDRs are reported. The measurements were taken from distinct samples. Because of the relatively small sample size of the trial, there was insufficient statistical power to formally adjust for multiple testing across the variety of comparisons relative to detecting small to moderate effect sizes. Although the findings based on different analyses were mutually supportive and biologically plausible, we acknowledge the limitation of the correlative analyses and emphasize that the corresponding results warrant further confirmation by larger-scale clinical or experimental studies. For the analysis of RNA-seq for gene expression changes, raw fastq files were mapped onto the hg38 human genome using the Spliced Transcripts Alignment to a Reference (STAR) aligner and gene level abundance was retrieved (57). PCA was performed on centered transcript data. DEGs for matched samples (*n* = 8) were calculated by doing a paired analysis with limma (58) by fitting a robust regression model to voom-transformed transcript amounts to identify significantly differentially expressed transcripts (FDR < 0.01 and log<sub>2</sub>FC > ±0.5; *n* = 1208). DEGs were then used to perform functional enrichment analysis using the ReactomePA package. The Trp signature used for gene set enrichment analysis was generated using data from KEGG (49, 59). Differential enrichment analysis was then performed, comparing the scores of the pre- versus posttreatment samples and visualized in R (55, 60, 61). Kaplan-Meier methods were used to generate time-to-event curves, from which survival proportions were calculated.

### SUPPLEMENTARY MATERIALS

[www.science.org/doi/10.1126/scitranslmed.abg8402](http://www.science.org/doi/10.1126/scitranslmed.abg8402)

Material and Methods

Figs. S1 to S11

Tables S1 to S8

Data file S1

MDAR Reproducibility Checklist

References (62–66)

[View/request a protocol for this paper from Bio-protocol.](#)

## REFERENCES AND NOTES

- D. H. Munn, A. L. Mellor, Indoleamine 2,3-dioxygenase and tumor-induced tolerance. *J. Clin. Invest.* **117**, 1147–1154 (2007).
- C. Uyttenhove, L. Pilotte, I. Theate, V. Stroobant, D. Colau, N. Parmentier, T. Boon, B. J. Van den Eynde, Evidence for a tumoral immune resistance mechanism based on tryptophan degradation by indoleamine 2,3-dioxygenase. *Nat. Med.* **9**, 1269–1274 (2003).
- D. H. Munn, M. D. Sharma, B. Baban, H. P. Harding, Y. Zhang, D. Ron, A. L. Mellor, GCN2 kinase in T cells mediates proliferative arrest and anergy induction in response to indoleamine 2,3-dioxygenase. *Immunity* **22**, 633–642 (2005).
- R. Metz, S. Rust, J. B. DuHadaway, M. R. Mautino, D. H. Munn, N. N. Vahanian, C. J. Link, G. C. Prendergast, IDO inhibits a tryptophan sufficiency signal that stimulates mTOR: A novel IDO effector pathway targeted by D-1-methyl-tryptophan. *Oncotargets Ther.* **1**, 1460–1468 (2012).
- F. Fallarino, U. Grohmann, K. W. Hwang, C. Orabona, C. Vacca, R. Bianchi, M. L. Belladonna, M. C. Fioretti, M. L. Alegre, P. Puccetti, Modulation of tryptophan catabolism by regulatory T cells. *Nat. Immunol.* **4**, 1206–1212 (2003).
- C. Smith, M. Y. Chang, K. H. Parker, D. W. Beury, J. B. DuHadaway, H. E. Flick, J. Boulden, E. Sutanto-Ward, A. P. Soler, L. D. Laury-Kleintop, L. Mandik-Nayak, R. Metz, S. Ostrand-Rosenberg, G. C. Prendergast, A. J. Muller, IDO is a nodal pathogenic driver of lung cancer and metastasis development. *Cancer Discov.* **2**, 722–735 (2012).
- J. Godin-Ethier, L. A. Hanafi, C. A. Piccirillo, R. Lapointe, Indoleamine 2,3-dioxygenase expression in human cancers: Clinical and immunologic perspectives. *Clin. Cancer Res.* **17**, 6985–6991 (2011).
- T. Inaba, K. Ino, H. Kajiyama, E. Yamamoto, K. Shibata, A. Nawa, T. Nagasaka, H. Akimoto, O. Takikawa, F. Kikkawa, Role of the immunosuppressive enzyme indoleamine 2,3-dioxygenase in the progression of ovarian carcinoma. *Gynecol. Oncol.* **115**, 185–192 (2009).
- F. Qian, J. Villlela, P. K. Wallace, P. Mhawech-Fauceglia, J. D. Tario Jr., C. Andrews, J. Matsuzaki, D. Valmori, M. Ayyoub, P. J. Frederick, A. Beck, J. Liao, R. Cheney, K. Moysich, S. Lele, P. Shrikant, L. J. Old, K. Odunsi, Efficacy of levo-1-methyl tryptophan and dextro-1-methyl tryptophan in reversing indoleamine-2,3-dioxygenase-mediated arrest of T-cell proliferation in human epithelial ovarian cancer. *Cancer Res.* **69**, 5498–5504 (2009).
- R. B. Holmgård, D. Zamarin, D. H. Munn, J. D. Wolchok, J. P. Allison, Indoleamine 2,3-dioxygenase is a critical resistance mechanism in antitumor T cell immunotherapy targeting CTLA-4. *J. Exp. Med.* **210**, 1389–1402 (2013).
- A. J. Muller, J. B. DuHadaway, P. S. Donover, E. Sutanto-Ward, G. C. Prendergast, Inhibition of indoleamine 2,3-dioxygenase, an immunoregulatory target of the cancer suppression gene Bin1, potentiates cancer chemotherapy. *Nat. Med.* **11**, 312–319 (2005).
- X. Liu, N. Shin, H. K. Koblish, G. Yang, Q. Wang, K. Wang, L. Leffert, M. J. Hansbury, B. Thomas, M. Rupar, P. Waeltz, K. J. Bowman, P. Polam, R. B. Sparks, E. W. Yue, Y. Li, R. Wynn, J. S. Fridman, T. C. Burn, A. P. Combs, R. C. Newton, P. A. Scherle, Selective inhibition of IDO1 effectively regulates mediators of antitumor immunity. *Blood* **115**, 3520–3530 (2010).
- G. L. Beatty, P. J. O'Dwyer, J. Clark, J. G. Shi, K. J. Bowman, P. A. Scherle, R. C. Newton, R. Schaub, J. Maleski, L. Leopold, T. F. Gajewski, First-in-human phase I study of the oral inhibitor of indoleamine 2,3-dioxygenase-1 epacadostat (INCB024360) in patients with advanced solid malignancies. *Clin. Cancer Res.* **23**, 3269–3276 (2017).
- T. C. Mitchell, O. Hamid, D. C. Smith, T. M. Bauer, J. S. Wasser, A. J. Olszanski, J. J. Luke, A. S. Balmanoukian, E. V. Schmidt, Y. Zhao, X. Gong, J. Maleski, L. Leopold, T. F. Gajewski, Epacadostat plus pembrolizumab in patients with advanced solid tumors: Phase I results from a multicenter, open-label phase I/II trial (ECHO-202/KEYNOTE-037). *J. Clin. Oncol.* **36**, 3223–3230 (2018).
- A. Daud, M. N. Saleh, J. Hu, J. S. Bleeker, M. J. Riese, R. Meier, L. Zhou, G. Serbest, K. D. Lewis, Epacadostat plus nivolumab for advanced melanoma: Updated phase 2 results of the ECHO-204 study. *J. Clin. Oncol.* **36**, 9511 (2018).
- G. V. Long, R. Dummer, O. Hamid, T. F. Gajewski, C. Caglevic, S. Dalle, A. Arance, M. S. Carlino, J. J. Grob, T. M. Kim, L. Demidov, C. Robert, J. Larkin, J. R. Anderson, J. Maleski, M. Jones, S. J. Diedo, T. C. Mitchell, Epacadostat plus pembrolizumab versus placebo plus pembrolizumab in patients with unresectable or metastatic melanoma (ECHO-301/KEYNOTE-252): A phase 3, randomised, double-blind study. *Lancet Oncol.* **20**, 1083–1097 (2019).
- A. J. Muller, M. G. Manfredi, Y. Zakharia, G. C. Prendergast, Inhibiting IDO pathways to treat cancer: Lessons from the ECHO-301 trial and beyond. *Semin. Immunopathol.* **41**, 41–48 (2019).
- C. A. Opitz, L. F. Somarribas Patterson, S. R. Mohapatra, D. L. Dewi, A. Sadik, M. Platten, S. Trump, The therapeutic potential of targeting tryptophan catabolism in cancer. *Br. J. Cancer* **122**, 30–44 (2020).
- J. G. Shi, K. J. Bowman, X. Chen, J. Maleski, L. Leopold, S. Yeleswaram, Population pharmacokinetic and pharmacodynamic modeling of epacadostat in patients with advanced solid malignancies. *J. Clin. Pharmacol.* **57**, 720–729 (2017).
- C. J. Martin, A. Datta, C. Littlefield, A. Kalra, C. Chapron, S. Wawersik, K. B. Dagbay, C. T. Brueckner, A. Nikiforov, F. T. Danehy Jr., F. C. Streich Jr., C. Boston, A. Simpson, J. W. Jackson, S. Lin, N. Danek, R. R. Faucette, P. Raman, A. D. Capili, A. Buckler, G. J. Carven, T. Schurpf, Selective inhibition of TGF $\beta$ 1 activation overcomes primary resistance to checkpoint blockade therapy by altering tumor immune landscape. *Sci. Transl. Med.* **12**, (2020).
- S. Spranger, R. Bao, T. F. Gajewski, Melanoma-intrinsic  $\beta$ -catenin signalling prevents anti-tumour immunity. *Nature* **523**, 231–235 (2015).
- S. C. Casey, L. Tong, Y. Li, R. Do, S. Walz, K. N. Fitzgerald, A. M. Gouw, V. Baylot, I. Gutgemann, M. Eilers, D. W. Felsher, MYC regulates the antitumor immune response through CD47 and PD-L1. *Science* **352**, 227–231 (2016).
- R. G. Verhaak, P. Tamayo, J. Y. Yang, D. Hubbard, H. Zhang, C. J. Creighton, S. Fereday, M. Lawrence, S. L. Carter, C. H. Mermel, A. D. Kostic, D. Etemadmoghadam, G. Saksena, K. Cubilskis, S. Duraisamy, K. Levanon, C. Sougnez, A. Tsherniak, S. Gomez, R. Onofrio, S. Gabriel, L. Chin, N. Zhang, P. Spellman, Y. Zhang, R. Akbani, K. A. Hoadley, A. Kahn, M. Kobel, D. Huntsman, R. A. Soslow, A. Defazio, M. J. Birrer, J. W. Gray, J. N. Weinstein, D. D. Bowtell, R. Drapkin, J. P. Mesirov, G. Getz, D. A. Levine, M. Meyerson; Cancer Genome Atlas Research Network, Prognostically relevant gene signatures of high-grade serous ovarian carcinoma. *J. Clin. Invest.* **123**, 517–525 (2013).
- M. E. Newman, Fast algorithm for detecting community structure in networks. *Phys. Rev. E* **69**, 066133 (2004).
- T. Eleftheriadis, G. Pissas, V. Liakopoulos, I. Stefanidis, IDO decreases glycolysis and glutaminolysis by activating GCN2K, while it increases fatty acid oxidation by activating AhR, thus preserving CD4 $^{+}$  T-cell survival and proliferation. *Int. J. Mol. Med.* **42**, 557–568 (2018).
- C. Canto, K. J. Menzies, J. Auwerx, NAD $^{+}$  metabolism and the control of energy homeostasis: A balancing act between mitochondria and the nucleus. *Cell Metab.* **22**, 31–53 (2015).
- O. A. Ulanovskaya, A. M. Zuhl, B. F. Cravatt, NNMT promotes epigenetic remodeling in cancer by creating a metabolic methylation sink. *Nat. Chem. Biol.* **9**, 300–306 (2013).
- E. Brunk, S. Sahoo, D. C. Zielinski, A. Altunkaya, A. Drager, N. Mih, F. Gatto, A. Nilsson, G. A. Preciat Gonzalez, M. K. Aurich, A. Prlic, A. Sastry, A. D. Danielsdottir, A. Heinken, A. Norrona, P. W. Rose, S. K. Burley, R. M. T. Fleming, J. Nielsen, I. Thiele, B. O. Palsson, Recon3D enables a three-dimensional view of gene variation in human metabolism. *Nat. Biotechnol.* **36**, 272–281 (2018).
- B. Hove-Jensen, K. R. Andersen, M. Kilstrup, J. Martinussen, R. L. Switzer, M. Willemoes, Phosphoribosyl diphosphate (PRPP): Biosynthesis, enzymology, utilization, and metabolic significance. *Microbiol. Mol. Biol. Rev.* **81**, (2017).
- H. R. Fernandez, S. M. Gadre, M. Tan, G. T. Graham, R. Mosaoa, M. S. Ongkeko, K. A. Kim, R. B. Riggins, E. Parasido, I. Petrini, S. Pacini, A. Cheema, R. Varghese, H. W. Ressom, Y. Zhang, C. Albanese, A. Uren, M. Paige, G. Giaccone, M. L. Avantaggiati, The mitochondrial citrate carrier, SLC25A1, drives stemness and therapy resistance in non-small cell lung cancer. *Cell Death Differ.* **25**, 1239–1258 (2018).
- O. Yanagida, Y. Kanai, A. Chairoungdua, D. K. Kim, H. Segawa, T. Nii, S. H. Cha, H. Matsuo, J. Fukushima, Y. Fukasawa, Y. Tani, Y. Takeuchi, H. Uchino, J. Y. Kim, J. Inatomi, I. Okayasu, K. Miyamoto, E. Takeda, T. Goya, H. Endou, Human L-type amino acid transporter 1 (LAT1): Characterization of function and expression in tumor cell lines. *Biochim. Biophys. Acta* **1514**, 291–302 (2001).
- F. Fallarino, U. Grohmann, P. Puccetti, Indoleamine 2,3-dioxygenase: From catalyst to signaling function. *Eur. J. Immunol.* **42**, 1932–1937 (2012).
- T. Duhen, R. Duhen, R. Montler, J. Moses, T. Moudgil, N. F. de Miranda, C. P. Goodall, T. C. Blair, B. A. Fox, J. E. McDermott, S. C. Chang, G. Grunkemeier, R. Leidner, R. B. Bell, A. D. Weinberg, Co-expression of CD39 and CD103 identifies tumor-reactive CD8 T cells in human solid tumors. *Nat. Commun.* **9**, 2724 (2018).
- A. Amobi-McCloud, R. Muthuswamy, S. Battaglia, H. Yu, T. Liu, J. Wang, V. Putluri, P. K. Singh, F. Qian, R. Y. Huang, N. Putluri, T. Tsuji, A. A. Lugade, S. Liu, K. Odunsi, IDO1 expression in ovarian cancer induces PD-1 in T cells via aryl hydrocarbon receptor activation. *Front. Immunol.* **12**, 678999 (2021).
- Y. Zhang, K. Bowman, J. Maleski, S. Diamond, S. Yeleswaram, Effects of epacadostat on brain extracellular fluid concentrations of serotonin—An intracerebral microdialysis study in Sprague-Dawley rats. *Drug Metab. Dispos.* **47**, 710–714 (2019).
- P. M. Sacramento, C. Monteiro, A. S. O. Dias, T. M. Kasahara, T. B. Ferreira, J. Hygino, A. C. Wing, R. M. Andrade, F. Rueda, M. C. Sales, C. C. Vasconcelos, C. A. M. Bento, Serotonin decreases the production of Th1/Th17 cytokines and elevates the frequency of regulatory CD4 $^{+}$  T-cell subsets in multiple sclerosis patients. *Eur. J. Immunol.* **48**, 1376–1388 (2018).
- C. Yang, B. Ko, C. T. Hensley, L. Jiang, A. T. Wasti, J. Kim, J. Suderth, M. A. Calvaruso, L. Lumata, M. Mitsche, J. Rutter, M. E. Merritt, R. J. DeBerardinis, Glutamine oxidation maintains the TCA cycle and cell survival during impaired mitochondrial pyruvate transport. *Mol. Cell* **56**, 414–424 (2014).
- A. Katoh, K. Ueno, M. Akita, T. Hashimoto, Early steps in the biosynthesis of NAD in Arabidopsis start with aspartate and occur in the plastid. *Plant Physiol.* **141**, 851–857 (2006).

39. S. G. Tullius, H. R. Biefer, S. Li, A. J. Trachtenberg, K. Edtinger, M. Quante, F. Krenzien, H. Uehara, X. Yang, H. T. Kissick, W. P. Kuo, I. Ghiran, M. A. de la Fuente, M. S. Arredouani, V. Camacho, J. C. Tigges, V. Toxavidis, R. El Fatimy, B. D. Smith, A. Vasudevan, A. El Khal, NAD<sup>+</sup> protects against EAE by regulating CD4<sup>+</sup> T-cell differentiation. *Nat. Commun.* **5**, 5101 (2014).
40. R. B. Brito, C. S. Malta, D. M. Souza, L. H. Matheus, Y. S. Matos, C. S. Silva, J. M. Ferreira, V. S. Nunes, C. M. Franca, H. Delle, 1-Methyl-D-tryptophan potentiates TGF-β-induced epithelial-mesenchymal transition in T24 human bladder cancer cells. *PLoS ONE* **10**, e0134858 (2015).
41. P. Pissios, Nicotinamide N-methyltransferase: More than a vitamin B3 clearance enzyme. *Trends Endocrinol. Metab.* **28**, 340–353 (2017).
42. M. A. Eckert, F. Coscia, A. Chryplewicz, J. W. Chang, K. M. Hernandez, S. Pan, S. M. Tienda, D. A. Nahotko, G. Li, I. Blazenovic, R. R. Lastra, M. Curtis, S. D. Yamada, R. Perets, S. M. McGregor, J. Andrade, O. Fiehn, R. E. Moellering, M. Mann, E. Lengyel, Proteomics reveals NNMT as a master metabolic regulator of cancer-associated fibroblasts. *Nature* **569**, 723–728 (2019).
43. G. Chakrabarti, D. E. Gerber, D. A. Boothman, Expanding antitumor therapeutic windows by targeting cancer-specific nicotinamide adenine dinucleotide phosphate-biogenesis pathways. *Clin. Pharmacol.* **7**, 57–68 (2015).
44. A. Chiarugi, C. Dolle, R. Felici, M. Ziegler, The NAD metabolome—A key determinant of cancer cell biology. *Nat. Rev. Cancer* **12**, 741–752 (2012).
45. A. von Heideman, A. Berglund, R. Larsson, P. Nygren, Safety and efficacy of NAD depleting cancer drugs: Results of a phase I clinical trial of CHS 828 and overview of published data. *Cancer Chemother. Pharmacol.* **65**, 1165–1172 (2010).
46. R. Kristeleit, I. Davidenko, V. Shirinkin, F. El-Khouly, I. Bondarenko, M. J. Goodheart, V. Gorburanova, C. A. Penning, J. G. Shi, X. Liu, R. C. Newton, Y. Zhao, J. Maleski, L. Leopold, R. J. Schilder, A randomised, open-label, phase 2 study of the IDO1 inhibitor epacadostat (INCB024360) versus tamoxifen as therapy for biochemically recurrent (CA-125 relapse)-only epithelial ovarian cancer, primary peritoneal carcinoma, or fallopian tube cancer. *Gynecol. Oncol.* **146**, 484–490 (2017).
47. J. Chong, D. S. Wishart, J. Xia, Using MetaboAnalyst 4.0 for comprehensive and integrative metabolomics data analysis. *Curr. Protoc. Bioinformatics* **68**, e86 (2019).
48. R. M. Wong, R. R. Scotland, R. L. Lau, C. Wang, A. J. Korman, W. M. Kast, J. S. Weber, Programmed death-1 blockade enhances expansion and functional capacity of human melanoma antigen-specific CTLs. *Int. Immunol.* **19**, 1223–1234 (2007).
49. M. Kanehisa, S. Goto, KEGG: Kyoto encyclopedia of genes and genomes. *Nucleic Acids Res.* **28**, 27–30 (2000).
50. G. Sales, E. Calura, D. Cavalieri, C. Romualdi, graphite—A Bioconductor package to convert pathway topology to gene network. *BMC Bioinformatics* **13**, 20 (2012).
51. C. Colijn, A. Brandes, J. Zucker, D. S. Lun, B. Weiner, M. R. Farhat, T. Y. Cheng, D. B. Moody, M. Murray, J. E. Galagan, Interpreting expression data with metabolic flux models: Predicting *Mycobacterium tuberculosis* mycolic acid production. *PLOS Comput. Biol.* **5**, e1000489 (2009).
52. M. K. Kim, A. Lane, J. J. Kelley, D. S. Lun, E-Flux2 and SPOT: Validated methods for inferring intracellular metabolic flux distributions from transcriptomic data. *PLOS ONE* **11**, e0157101 (2016).
53. L. Heirendt, S. Arreckx, T. Pfau, S. N. Mendoza, A. Richelle, A. Heinken, H. S. Haraldsdottir, J. Wachowiak, S. M. Keating, V. Vlasov, S. Magnusdottir, C. Y. Ng, G. Preciat, A. Zagare, S. H. J. Chan, M. K. Aurich, C. M. Clancy, J. Modamio, J. T. Sauls, A. Noronha, A. Bordbar, B. Cousins, D. C. El Assal, L. V. Valcarcel, I. Apaolaza, S. Ghaderi, M. Ahookhosh, M. B. Guebla, A. Kostromins, N. Sompairac, H. M. Le, D. Ma, Y. Sun, L. Wang, J. T. Turkovich, M. A. P. Oliveira, P. T. Vuong, L. P. El Assal, I. Kuperstein, A. Zinovyev, H. S. Hinton, W. A. Bryant, F. J. A. Artacho, F. J. Planes, E. Stalidzans, A. Maass, S. Vempala, M. Hucka, M. A. Saunders, C. D. Maranas, N. E. Lewis, T. Sauter, B. O. Palsson, I. Thiele, R. M. T. Fleming, Creation and analysis of biochemical constraint-based models using the COBRA Toolbox v.3.0. *Nat. Protoc.* **14**, 639–702 (2019).
54. C. Giesen, H. A. Wang, D. Schapiro, N. Zivanovic, A. Jacobs, B. Hattendorf, P. J. Schuffler, D. Grolimund, J. M. Buhmann, S. Brandt, Z. Varga, P. J. Wild, D. Gunther, B. Bodenmiller, Highly multiplexed imaging of tumor tissues with subcellular resolution by mass cytometry. *Nat. Methods* **11**, 417–422 (2014).
55. R Core Team, R: A language and environment for statistical computing (2021); www.R-project.org/.
56. F. Hahne, N. LeMeur, R. R. Brinkman, B. Ellis, P. Haaland, D. Sarkar, J. Spidlen, E. Strain, R. Gentleman, flowCore: A Bioconductor package for high throughput flow cytometry. *BMC Bioinformatics* **10**, 106 (2009).
57. A. Doba, C. A. Davis, F. Schlesinger, J. Drenkow, C. Zaleski, S. Jha, P. Batut, M. Chaisson, T. R. Gingras, STAR: Ultrafast universal RNA-seq aligner. *Bioinformatics* **29**, 15–21 (2013).
58. M. E. Ritchie, B. Phipson, D. Wu, Y. Hu, C. W. Law, W. Shi, G. K. Smyth, limma powers differential expression analyses for RNA-sequencing and microarray studies. *Nucleic Acids Res.* **43**, e47 (2015).
59. A. Subramanian, P. Tamayo, V. K. Mootha, S. Mukherjee, B. L. Ebert, M. A. Gillette, A. Paulovich, S. L. Pomeroy, T. R. Golub, E. S. Lander, J. P. Mesirov, Gene set enrichment analysis: A knowledge-based approach for interpreting genome-wide expression profiles. *Proc. Natl. Acad. Sci. U.S.A.* **102**, 15545–15550 (2005).
60. Z. Gu, R. Eils, M. Schlesner, Complex heatmaps reveal patterns and correlations in multidimensional genomic data. *Bioinformatics* **32**, 2847–2849 (2016).
61. H. Wickham, *ggplot2: Elegant Graphics for Data Analysis* (Springer-Verlag New York, 2016).
62. H. K. Koblish, M. J. Hansbury, K. J. Bowman, G. Yang, C. L. Neilan, P. J. Haley, T. C. Burn, P. Waelz, R. B. Sparks, E. W. Yue, A. P. Combs, P. A. Scherle, K. Vaddi, J. S. Fridman, Hydroxyamidine inhibitors of indoleamine-2,3-dioxygenase potently suppress systemic tryptophan catabolism and the growth of IDO-expressing tumors. *Mol. Cancer Ther.* **9**, 489–498 (2010).
63. M. I. Love, W. Huber, S. Anders, Moderated estimation of fold change and dispersion for RNA-seq data with DESeq2. *Genome Biol.* **15**, 550 (2014).
64. G. Csardi, T. Nepusz, The igraph software package for complex network research. *InterJournal Complex Systems*, 1695 (2006).
65. R. Catena, L. M. Montuenga, B. Bodenmiller, Ruthenium counterstaining for imaging mass cytometry. *J. Pathol.* **244**, 479–484 (2018).
66. L. van der Maaten, G. Hinton, Visualizing data using t-SNE. *J. Mach. Learn. Res.* **9**, 2579–2605 (2008).

**Acknowledgments:** This work used the following shared resources at the Roswell Park Comprehensive Cancer Center supported by P30CA016056: Pathology Resource Network, Genomics, Flow Cytometry, Biostatistics, Bioinformatics, and Immune Analysis. This work also used core facilities at Dan L. Duncan Cancer Center, Baylor College of Medicine (P30CA125123): Metabolomics Core, CPRIT Proteomics, and Metabolomics Core Facility (RP170005). **Funding:** This study was supported by U01CA154967 to M.A.C. and S.P.F.; Cancer Center Support grant P30CA015704 to M.A.C. and S.P.F.; Swiss National Science Foundation (grant numbers 163390 and 176279) to R.G.; U01CA230385 to K.O.; U24CA232979 to K.O.; an NIH administrative supplement to Roswell Park-UPCI Ovarian Cancer SPORE P50CA159981-01A1 to K.O.; R01CA216426, R01CA220297, U01CA214263, and the American Cancer Society (127430-RSG-15-105-01-CNE) to N.P.; and University of Chicago Medicine Comprehensive Cancer Center Support Grant P30CA014599 to K.O. **Author contributions:** K.O., M.A.G., S.P.F., and M.A.C. contributed to the conceptualization. K.O., J.C.K., J.M., C.M., M.L.D., C.D.M., and S.P.F. contributed to the clinical trial design and biospecimen collection. K.O., M.A.G., S. Lele, E.Z., and M.A.C. conducted the clinical trial. A.M.L., J.C.K., S.P.F., N.R., and A.A.L. contributed to data curation. J.M., T.T., L. D'Amico, L. Dennis, P.D., S.W., V.A.N., D.E.M., S. Ravi, R.G., V.P., N.P., and F.Q. contributed to methodology. H.Y., W.Z., S. Liu, S.B., S. Rosario, R.S., R.G., V.P., N.P., and F.Q. contributed to omic data generation and/or processing. F.Q. performed mouse model experiments. F.Q., A.J.R.M., J.C., S.B., and K.O. analyzed the data. H.Y., S.B., W.Z., V.A.N., D.E.M., R.S., R.G., V.P., N.P., A.A.L., A.H., R.K., and K.O. contributed to formal analysis of clinical omics, metabolomics, toxicity, and survival data as well as preclinical omics data and PK/PD modeling. K.O., J.M., A.A.L., S.P.F., T.C., J.C.K., N.R., and M.A.C. contributed to project administration. K.O. and M.A.C. contributed to supervision. K.O., M.A.G., S.P.F., M.A.C., V.A.N., D.E.M., R.S., R.G., H.Y., S.B., W.Z., F.Q., J.M., and A.A.L. wrote the original draft of the paper.

**Competing interests:** K.O. is a cofounder of Tactiva Therapeutics and receives research support from AstraZeneca and Tesaro. R.K. is a cofounder of Tactiva Therapeutics, and R.K. engaged in past or current consulting for Terumo BCT, Costar, and Medicago. L. Dennis, P.D., and S.W. declare that they are employees and shareholders of NanoString Technologies. A.J.R.M. is a paid consultant for Cellular Analytics Inc., which is developing TIL-based therapies for cancer. D.E.M. is the president and CEO of Enhanced Pharmacodynamics LLC. C.D.M. has held restricted stock in OmniSeq. C.M. is a paid consultant for Merck for a vaccine product. The other authors declare that they have no competing interests. **Data and materials availability:** Raw and processed RNA-seq data are available at the Gene Expression Omnibus Hub with accession number GSE155164. The following information was uploaded to Zenodo DOI: doi.org/10.5281/zenodo.6112448: processed data and code used to process RNA-seq, CyTOF, flow cytometry, metabolic studies, NanoString, and PK/PD data, as well as raw CyTOF and flow cytometry files. Raw IMC/mcd files have been uploaded to Synapse at this link: www.synapse.org/#!Synapse:syn27088468/files/.

Submitted 2 February 2021  
Resubmitted 31 October 2021  
Accepted 24 February 2022  
Published 16 March 2022  
10.1126/scitranslmed.abg8402